Delft University of Technology

MSc Nanobiology

Master Thesis

Characterizing the architecture of reconstituted minimal septin and septin-actin cortices at high resolution

Author:
BSc Djim de Ridder
4441362

January 4, 2021 - January 29, 2022

Daily Supervisors:
MSc. Gerard Castro-Linares [1]
MSc. Lucia Baldauf[1]

Supervisor and examiner:
Prof. dr. Gijsje H. Koenderink[1]
Second examiners:
Dr. Arjen Jakobi[1]
Dr. Timon Idema[1]

[1]Department of Bionanoscience, Kavli Institute of Nanoscience Delft, Delft University of Technology, Delft, Netherlands

1 Abstract

In animal cells, cell shape is primarily regulated by the actin cortex, a thin filament network connected to the plasma membrane. The architecture of the cortex is considered a key regulator of its function. Visualising the cortex is difficult due to the high density of numerous small-sized proteins involved in its formation. Consequently, the structure of the cortex at the membrane remains poorly studied. This study aims to gain insight into the organisation at the membrane of two key cortical components, human septin and septin-recruited actin. To study these filament structures, we reconstitute minimal cortices on supported lipid layers as model-membranes, allowing for imaging with electron and atomic force microscopy. We show that membrane binding of human septin results in ordered organisations of filaments. However, we find septin organises into arrays of paired filaments when incubated on a lipid monolayer and networks of bundles when incubated on a lipid bilayer. In addition, we showed a proof of concept for actin cortex reconstitution on lipid monolayers, which allowed us to see actin recruitment by septin meshworks.

Contents

2 Introduction

2.1 Motivation and aim

Cells are isolated from the environment through a deformable lipid membrane. This lipid membrane needs to be flexible to allow the cell to change shape but also rigid enough to face mechanical challenges from their environment. This requires the cell to have robust but adaptive machinery to control its shape. A key part of that machinery is the cortex, which plays a significant role in shaping the animal cell by controlling the surface tension, membrane curvature, and protrusion formation [1–3].

The actin cortex is a thin layer of cytoskeletal proteins connected to the cell membrane. The cortex comprises actin and actin-binding proteins, including the filamentous cytoskeletal protein septin. The structure of the cortex plays a crucial part in cortex function [4]. However, the cortex is a complex system to study due to its small size scale, high-density meshworks, and the large number of proteins involved [5]. For this reason, the cortex's architecture at the cell's surface remains poorly understood.

In this project, we focus on the filamentous cytoskeletal protein septin. Septin has been reported to be localised to the cell membrane, where it can interact with phospholipids and other proteins [6]. While recent studies show septin function in membrane curvature [7, 8], septin has also been thought to recruit proteins such as actin at the interface of the cortex and the cell membrane. We investigate how human septin is organised at the cell membrane and how septin recruits and organises actin at the cell membrane.

Reconstitution of the cortex allows for minimal simplified models used to study the biological role of individual proteins. We used supported lipid layers as model-membrane systems to see organisation at the membrane. Supported lipid bilayers are often used in combination with light microscopy to study cortical dynamics. However, light microscopy can not resolve individual filaments in dense protein networks like the septin meshworks [9].

To study the mechanics of mammalian septins interactions with the plasma membrane, we aim to gain an understanding of human septin organisation on model membranes. To this end, we imaged reconstituted cortices with negative stain transmission electron microscopy (TEM) and atomic force microscopy (AFM). To this end, we used a methodology previously used to study fly septin [9]. Our second aim is to expand on the electron microscopy method to investigate actin recruitment of membrane-bound human septin. The actin networks formed using this method were compared to similarly imaged Arp2/3 nucleated actin networks. Showing actin recruitment with this method would demonstrate that this methodology can reveal the structure of other minimal cortical networks.

This thesis is divided into five chapters focused on different aspects of the study. In the remainder of chapter 2, we describe the current knowledge of septin in the actin cortex in more detail. We will first introduce the plasma membrane and the cytoskeleton. Next, we will focus on the actin cortex. We will then review the used model-membrane systems and how these are used to reconstitute and study the cortex. In chapter 3 the materials used and methods are described. Next, in chapter 4, the results of the experiments will be explained and discussed. After that, in chapter 5, we will compare the results. And finally, in chapter 6, we summarise our findings and place them in the broader context of the field.

2.2 Background

2.2.1 Plasma membrane

The plasma membrane surrounds the cell. It acts as a physical barrier separating the inside from the outside of the cell. The membrane is semi-permeable, which means that the membrane acts as a gatekeeper admitting only specific substances into the cell. Furthermore, the membrane is involved in cell signalling and regulates transport. In this thesis, however, we will focus on the membrane's function as the biochemical environment at the boundary of the cell.

The plasma membrane consists of a double layer of lipids, a lipid bilayer, embedded with proteins (figure 1A). The embedded proteins either go across the bilayer or attach to the inner or outer leaflet. These proteins are responsible for a variety of biological processes in the cell. Furthermore, the bilayer consists of two lipid layers, often referred to as the inner and outer leaflets (figure 1B). The lipid leaflets consist of hundreds of different lipids [10] which can diffuse within the lipid bilayer [11]. While other lipid types also play an important role in the plasma membrane, the lipid bilayer is primarily composed of glycerophospholipids [11, 12].

2.2.1.a Glycerophospholipids

Glycerophospholipids serve as the membrane's structural component. They comprise a hydrophobic tails region connected to the hydrophilic head via a glycerol group (figure 1C). The headgroup contains a phosphate ester. The headgroup becomes hydrophilic because it is polar, allowing for interactions with surrounding water molecules. The tail region consists of two fatty acids. Since the tail group consist of only apolar molecules, no hydrogen bonds are formed, rendering the tail hydrophobic. Because of the amphipathic nature of these lipids, they spontaneous form lipid bilayers in an aqueous surrounding to cage the hydrophobic tail from the water molecules [11].

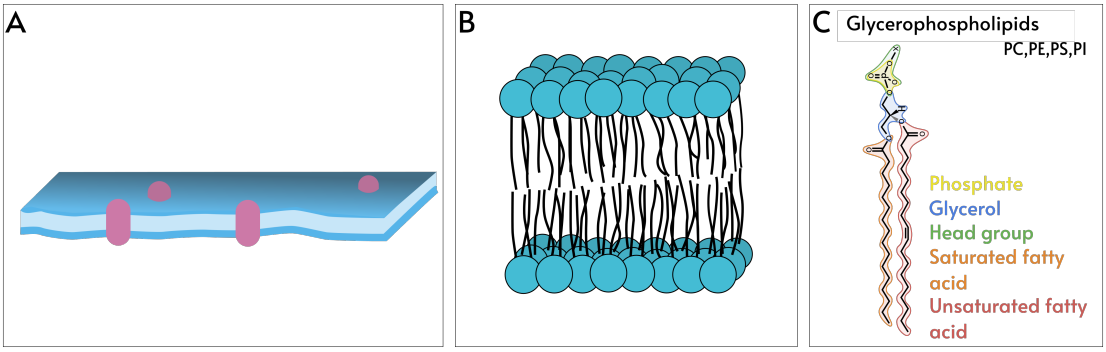

Figure 1: **Overview of plasma membrane.**(A) A simplified representation of the plasma membrane consisting of a lipid bilayer membrane with embedded proteins. (B) A zoom-in of the phospholipid bilayer. (C) The molecular structure for glycerophospholipids.

The most common lipids in mammalian cell membranes include phosphatidylcholine (PC), phosphatidylethanolamine (PE), and phosphatidylserine (PS). These lipids are differentiated based on their head group. For example, while PC and PE are neutral, PS lipids carry a net negative charge. Phosphatidylinositol (PI) is another membrane lipid class with a negative charge. The PI lipid can be phosphorylated, adding up to three phosphates to the structure. An example of a lipid formed from this phosphorylation is phosphatidylinositol 4,5-bisphosphate (PIP_2), which has a net charge of -4 at neutral pH [13]. The headgroup is exposed to the aqueous environment, which allows the membrane to interact with the surrounding (figure 1B). In addition, specific proteins can bind to particular headgroups, and various proteins can only function in the presence of a particular phospholipid, making the lipids' composition regulate cellular processes such as cell signalling [11]. These properties make lipid headgroups essential for specific functions. For example, the head group of PIP_2 plays an important signalling role during cell division [14].

2.2.2 The Cytoskeleton

The eukaryotic cytoskeleton is a complex network composed of biopolymers that provides mechanical support to the cell (figure 2A). Furthermore, the cytoskeleton also provides pathways for transportation inside the cell and controls the cell's shape while also maintaining its mechanical integrity. Controlling the cell structure is necessary for cell growth, division and migration. The cytoskeletal filaments are microtubules, actin, and intermediate filaments. More recently, septin has been recognised as another key cytoskeletal component [6]. These components are biopolymers that form filaments organised in higher-order structures, such as bundles, networks or tubes. Furthermore, septin and actin, in particular, have been shown to interact closely with the cell membrane (figure 2B) [8, 15]. However, the exact roles of different proteins in this interaction are still poorly understood. The following section will introduce septin and actin, the two filaments studied in this project.

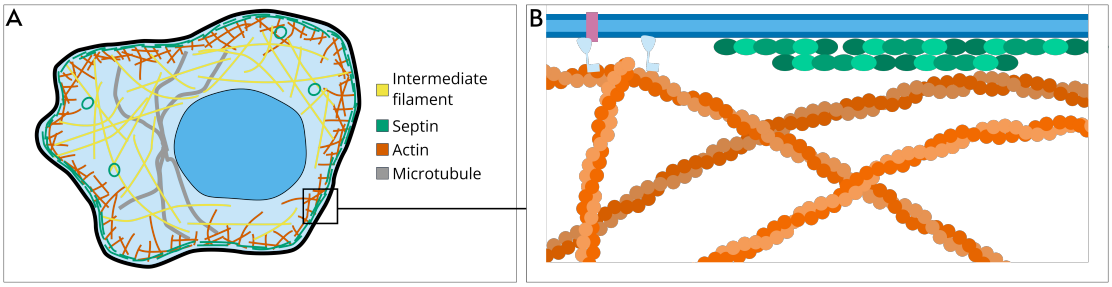

Figure 2: **Overview of cytoskeleton.** (A) A representation of the four filaments inside the cell. (B) An illustration of the actin cortex at the plasma membrane.

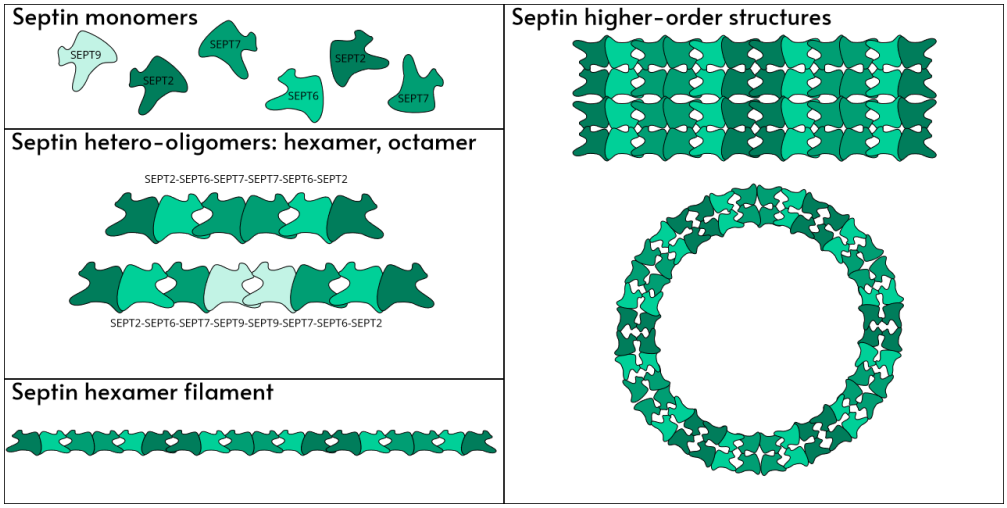

Figure 3: **Overview of human septin organisations.** Subunits of septin can polymerise in a hexamer or octamer configuration. These hetero-oligomers can form filaments, which in turn can form higher order structures

2.2.2.a Septin

Septins are a group of proteins that can polymerise into hetero-oligomeric complexes (figure 3). These hetero-oligomers can polymerise into filaments by end-to-end annealing [16]. Subsequently, these filaments can be organised into higher-order assemblies like straight bundles, rings, or cage-like formations [17], as shown in figure 3. These configurations allow septin to regulate localised cellular processes at the cleavage furrow and plasma membrane [6]. For instance, at the cleavage furrow in yeast, septin acts as a diffusive barrier to compartmentalise the plasma membrane [18, 19]. Septins have also been shown to be necessary for the formation of the cytokinetic ring [7].

There are two active hetero-oligomers the human septin family can form: septin hexamers and septin octamers. The septin subunits assemble by alternating G and NC-interfaces [16]. The current model for the hexamer subunit arrangement has Sept7 at the centre followed by Sept6, with finally Sept2 on the exterior, with its NC-interface facing outward [20, 21]. Human octamers subunit order from the centre to the outside is Sept9, Sept7, Sept6 and Sept 2 (figure 3). Since Sept2 is on the outside of both hetero-oligomers, hexamers and octamers can copolymerise [22].

Yeast septin has been shown to organise on lipid membranes containing PIP_2, forming meshwork structures [23], while human septin has only been shown to bind to PIP_2 [24]. While septin can bind to locally flat membranes [25], it has also been shown to have a micron-scale curvature sensing [8, 26], and curvature generating ability [8]. Septin also colocalises with actin and microtubules [27].

2.2.2.b Actin

Actin is well conserved and highly abundant in eukaryotes and plays a role in essential cell functions such as protein transport, cell migration, structure, and division [28–30].

Actin is a globular monomer (G-actin) that can polymerise into helical actin filaments (F-actin) by ATP hydrolysis. G-actin polymerises into F-actin in a head to tail manner under physiological circumstances [31]. The actin monomers combine to form a 7-nm polar filament made up of two parallel twisting protofilaments. In cells, actin nucleation factors are necessary to promote polymerisation, such as the Arp2/3 complex [32]. Furthermore, the turnover of actin is highly regulated. In solution, actin filaments can polymerise and depolymerise at both ends; however, F-actin is preferentially assembled at the plus end and disassembled at the minus end [31].

Actin-binding proteins (ABP) are a group of proteins that interact with actin. ABPs are involved in regulating actin polymerisation and depolymerisation, nucleating actin and organising actin filaments into higher-order structures [33]. Actin filaments can be organised in a diverse range of higher-order structures, forming bundles and filament networks. Interactions with the membrane influence the architecture of such actin structures through ABPs, which anchor actin to the membrane.

2.2.3 The Actin cortex

Actin filaments form a network at the inner face of the membrane called the actin cortex. In addition to actin filaments, the cortex is composed of hundreds of different ABP [5]. The actin cortex is a part of the cytoskeleton that regulates membrane tension, which is necessary for driving shape changes [34]. The cortex also controls cell shape by regulating the turnover of actin filaments, and contraction of the filaments by the motor protein myosin [34, 35]. Furthermore, the cortex provides the cell mechanical stability and cell surface rigidity [36].

The architecture of the actin cortical network influences mechanics and function [4]. The cortex can be regulated to form a diverse range of structures. This structural control allows the cortex to perform different functions for different cells and under different conditions [35]. For example, the cortex is composed of densely branched networks in migrating cells for generating pushing force [37]. While in dividing cells, the cortex forms ordered filaments to promote constriction of the cell's midplane [38].

A key ABP at the cortex for cell protrusion is the Arp2/3 complex [35, 39]. Interaction between Arp2/3 and VCA is what drives the formation of branched actin networks [39]. Arp2/3 binds pre-formed actin filaments and nucleates a new filament at a 70°angle with respect to the pre-formed filament [40]. However, the Arp2/3 complex by itself is inefficient and requires a nucleation promotion factor with a VCA domain [41]. The VCA domain is a functional domain of N-WASP, WASP and WAVE, which are scaffolding proteins that link actin to the membrane.

Septin is also located in the cortex [6]. Septin is important for regulating cortical rigidity [36]. Furthermore, septin may also play a crosslinking or recruiting role for actin at the plasma membrane [42, 43]. By itself, septin can bind lipid membranes forming networks that could reinforce or deform the membrane [23, 25]. Reinforcement of the membrane by septin could explain the difference in membrane tension in actin disassembled fibroblast cells compared to lipid vesicles [44]. Little is known yet about septin's influence on the actin organisation at the cortex.

2.3 Reconstituted actin cortex

Over a hundred different ABPs are found in the cortex [5], structuring cortical actin filaments as a dense crosslinked meshwork linked to the plasma membrane. And since the actin forms dense networks of filaments of 7 nm in diameter, it is difficult to study the cortex with traditional light microscopy. However, molecular players in the cortex have been identified [45–47] which allowed in vitro bottom-up reconstitution studies. Minimal cortex systems have been used to study the dynamic and structure of the cortex [4].

2.4 Membrane models

Membrane models are used to mimic the plasma membrane. Membrane models often consist of only a few types of glycerophospholipids compared to the plasma membranes, with many components [10, 11] that are speculated to form domains with specific characteristics [48]. The three main membrane models often used to study membrane-protein interaction are lipid monolayers, lipid vesicles, and supported lipid bilayers. For this project, we will use both lipid monolayers, and lipid bilayers [49].

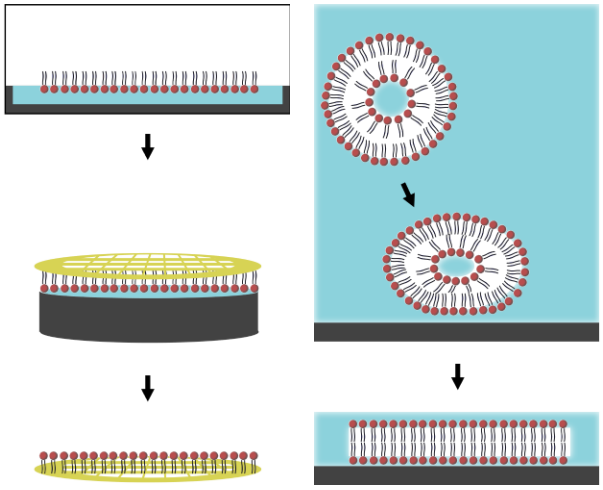

Figure 4: **Schematic overview of membrane model formation.** (Left) Overview of lipid monolayer transfer method for TEM-grid-supported lipid monolayers. (Right) Small unilamellar vesicles fusion to supported lipid bilayers.

2.4.1 Supported lipid bilayers

Supported lipid bilayers (SLB) are flat membranes on a solid substrate held together by hydrophobic interactions between the lipids. Lipid bilayers are regularly used as models to study cortical networks [25, 50]. SLBs can be produced in different ways [49, 51]. We chose small unilamellar vesicles (SUV) fusion, a method where lipid vesicles spread on a hydrophilic surface (figure 4A). A flat substrate is also essential since we will use AFM as our high-resolution imaging method for these models. If the substrate is not flat, we will measure the substrate inconsistencies due to the high axial resolution of AFM.

2.4.2 Supported lipid monolayers

For TEM, we need to reconstitute the cortex on an EM-grid. While supported lipid bilayers are more similar to the plasma membrane, it is challenging to form EM-grid-supported lipid bilayers [52, 53]. However, EM-grid supported lipid monolayers, often used to determine the structure of membrane-binding proteins [54], are also used for studying cytoskeleton protein organisation at the membrane [23, 25]. For this reason, we used a lipid monolayer for the cortex model we imaged with EM.

3 Materials and methods

This research project consisted of experiments using in vitro models of filament networks on top of supported lipid membranes. The reconstituted networks studied in this project were composed of septin alone, septin with actin, or Arp2/3-VCA polymerised actin. We used substrates suited to the imaging technique to build our supported lipid membranes. This section describes the general methods and materials for the assays utilised in this research.

3.1 Proteins and buffers

Buffers During our experiment, we kept the proteins and lipids in buffers. In the table below (table 1), we have listed an overview of buffers.

Components	**G-buffer**	**S-buffer**	**F-buffer**	**NaCi-buffer**	**imaging-buffer**	**polymerisation-buffer**
KCl		300 mM	50 mM	50 mM	50 mM	50 mM
$MgCl_2$		2 mM	2 mM		2.4 mM	2.4 mM
dithiothreitol (DTT)	1 mM	1 mM	1 mM		1 mM	1 mM
tris(hydroxymethyl)aminomethane hydrochloride (Tris-HCl) pH 7.8	5 mM					
Tris-HCl pH 7.4		20 mM	20 mM		24.2 mM	24.2 mM
adenosine 5'-triphosphate magnesium salt (MgATP)	0.2 mM					
$CaCl_2$	0.1 mM					
citrate (2:3 trisodium citrate : citric acid)				50 mM		
ethylenediaminetetraacetic acid (EDTA)				0.1 mM		
6-hydroxy-2,5,7,8-tetramethylchroman-2-carboxylic acid (Trolox)					1 mM	
protocatechuic acid (PCA)					1 mM	
protocatechuate 3,4-dioxygenase (PCD)					0.05 µM	

Table 1: **Buffer components.**

Actin
We performed experiments with Lyophilised monomeric actin (G-actin) from rabbit skeletal muscle (8101-03, Hypermol). First, the protein was resuspended according to the supplier's protocol. Next, the actin is dialysed against G-buffer and spun down for one hour at 148000g. The actin was stored in G-buffer at -80 °C. The actin stays mostly in monomeric form when stored in G-buffer. For that reason, the aliquots of actin were thawed and kept on ice for two hours before being spun down in an Airfuge at 30 psi (Airfuge Ultracentrifuges, Beckman-Coulter) to remove any aggregated actin. After the aliquot spun down, we kept it on ice or in a -4 °C fridge for up to two weeks.

Septin
For this project, we used two septin oligomers, human septin hexamers and human septin octamers, with one specific Septin 9 isoform (SEPT9_i1). In-house purification protocols were used, where the septin hetero-oligomers were expressed in *E. coli* BL21 (DE3) [55, 56]. Septin is purified with nickel affinity chromatography using the 6His-tag fused to the SEPT2 subunit. The septins were stored in S-buffer at -80 °C. Before use, the septins were diluted in S-buffer and kept on ice or in a -4 °C fridge.

For fluorescence microscopy, a mix was made from dark septin and 10 mole% fluorescent septin complexes. The fluorescent septin contains a monomeric superfolder green fluorescent protein (msGFP) fused to the C-terminus of SEPT2.

Arp2/3
We purchased Arp2/3 complex from porcine brain (8413-01, Hypermol). We followed the supplier's instructions for dissolving and storing the complex. After the protein is dissolved we snap-freeze, aliquote and store it at -80 °C in storage buffer (150mM KCl, 1mM $MgCl_2$, 1 mM DTT, 20mM Tris pH 7.5, 0.2mM ATP, 0.5mM Ethylenediaminetetraacetic acid (EDTA), 5% disaccharides). We immediately used the protein after thawing.

VCA
A plasmid to purify 10×His-tagged VCA domain (murine N-Wasp) was a kind gift from Dr. Kristina Ganzinger. We purified the protein by following a previously described protocol [57]. First, the protein was purified from E. coli by nickel affinity chromatography followed by anion exchange chromatography. After purification, the protein was kept in storage-buffer (200mM KCl, 4mM $MgCl_2$, 5 mM DTT, 20mM Tris pH 7.4), aliquoted, snap-frozen and stored at -80 °C. We immediately used the protein after thawing.

Lipids
We purchased all lipids from Avanti Polar Lipids (table 2). Most lipids were kept at -20 °C dissolved in chloroform and stored under argon. However, PIP_2 was kept in a mixture of chloroform : methanol : water in a volume ratio of 20:9:1.

Abbreviation	**Name**	**Catalog number**
DOPC	18:1 1,2-dioleoyl-sn-glycero-3-phosphocholine	850375
DOPS	18:1 1,2-dioleoyl-sn-glycero-3-phospho-L-serine	840035
PI	18:1 1,2-dioleoyl-sn-glycero-3-phospho-(1'-myo-inositol)	850149
PIP_2	18:1 1,2-dioleoyl-sn-glycero-3-phospho-(1'-myo-inositol-4',5'-bisphosphate)	850155
DGS-NTA(Ni)	18;1 1,2-dioleoyl-sn-glycero-3-[(N-(5-amino-1-carboxypentyl)iminodiacetic acid)succinyl]	790404
Cy5-PE	18:1 1,2-dioleoyl-sn-glycero-3-phosphoethanolamine-N-(Cyanine 5)	810335

Table 2: **Lipid details.**

Multi-component lipid membranes were prepared at room temperature by mixing the different components in glass vials (1.5 mL glass vial, VWR) or glass test tubes (Pyrex test tube 12×75 medium walls, Pyrex) in chloroform or a mixture of chloroform : methanol : water in a volume ratio of 20:9:1 when PIP_2 was in the lipid mix. Before use, the glass test tubes were sequentially cleaned with soap, acetone, ethanol, and MilliQ water.

To prepare small unilamellar vesicles (SUVs), we evaporated the chloroform in the lipid mixtures by drying them with nitrogen gas after mixing the lipids in glass test tubes. Next, we removed any further traces of solvent by placing the dried mixtures in a vacuum for at least 3 hours (overnight for mixture with PIP_2). The dried lipid films are resuspended in F-buffer or NaCi-buffer. We used F-buffer to resuspend lipids without PIP_2 while using NaCi buffer for lipids with PIP_2. After that, we promoted SUV formation by first exposing the lipids to 12 freeze-thaw cycles and sequentially sonicating the lipids. We used a SONOPULS HD 2070.2 Ultrasone homogeniser (Bandelin) with a BR30 cup-horn sonicator (Bandelin) to sonicate the mixture at room temperature for 1 hour in pulse mode (5s on/5 s off) with 20% output intensity.

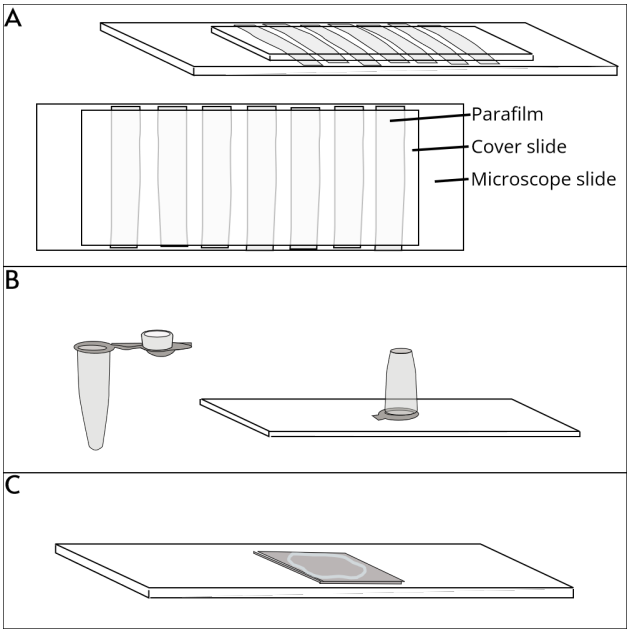

Figure 5: **Devices with a hydrophilic substrate for supported lipid bilayer formation.** (A) Flow channel assembled by melting Parafilm between a base piranha treated cover slide and base piranha treated microscope slide. (B) Chamber made out of a PCR tube glued to a treated coverslip. (C) Base piranha treated silicon wafer glued to a microscope slide. A ring of grease acts as a hydrophobic barrier to contain the sample

3.2 Supported lipid bilayers formation

The supported lipid bilayers (SLBs) are formed by SUV fusion, where small lipid vesicles coat a hydrophilic surface [58, 59]. We used either glass or silicon wafers.

Glass pretreatment
To form an SLB, we need a hydrophilic surface that is contaminant free. To make glass hydrophilic and contaminant-free, we cleaned the glass slides with base-piranha (5:1:1 MilliQ water : 30% hydrogen peroxide (Sigma-Aldrich) : 30% ammonium hydroxide (Sigma-Aldrich)). We treated both microscope slides (76 x 26 mm, thickness: 0.1mm, Menzel Gläser) and cover slides (24 x 60 mm, thickness: 0.15mm, Menzel Gläser) used for our devices on which we formed glass-supported lipid bilayers. First, we prepared 210 mL base-piranha inside a 250 mL glass beaker in a fume hood. Next, the reaction is initiated by heating the mixture to at least 70°C with a hot plate. After the reaction is initiated (indicated by bubbling), we immersed the glass slide held by a Teflon rack for 10 minutes inside the solution. After washing the slides with MilliQ water at least three times, we stored the glass in MilliQ water at room temperature for up to 3 days.

Device preparation
The flow channels were prepared by placing Parafilm strips (Bemis) between a microscope slide (76 x 26 mm, thickness: 0.1mm, Menzel Gläser) and a cover slide (24 x 60 mm, thickness: 0.15mm, Menzel Gläser) (Figure 5A). The strips (2-4 mm) were spaced 2-4 mm apart. After assembly, the device is briefly heated on a hotplate to melt the Parafilm and form watertight channels.

The flow channel is brought to room temperature and used no longer than 15 minutes after assembly. The channels of around 10 µL can be accessed from two sides. We created a flow by pipetting a solution from one side and forming a suction force from the other with dry tissue paper. The flow channel is used at room temperature, and F-buffer is placed at both ends of the channel to prevent drying.

The chambers were assembled by glueing a PCR tube (AB0620, Thermo Scientific) to a cleaned cover slide (24 x 60 mm, thickness: 0.15mm, Menzel Gläser) with two-component epoxy glue (Bison Kombi Snel-rapide) (Figure 5B). These chambers can hold around 150 µL, but we used 30 µL to comfortably cover the bottom of the chamber. We accessed the chambers from above with a pipette tip. In addition, we exchanged the solution inside the chamber by repeatedly removing half the volume before refilling the chamber.

SLB formation
We assemble the glass-supported lipid bilayers at room temperature by adding the SUVs in a salt buffer (F-buffer or NaCi-buffer) to the devices. After 30 minutes, the unbound vesicles are removed by flushing the channels or exchanging the chambers with 3× its volume.

3.2.1 Silicon wafer-supported lipid bilayers

For AFM, we used silicon wafers as our substrate for SLB supported reconstituted cortices. Silicon wafers consist of monocrystalline silicon and can be treated with UV/ozone to render the surface hydrophilic.

We purchased silicon wafers with a thickness of ˜525 µm (BT electronics). The wafer is cut into 10×10 mm^2 squares, sequentially rinsed with MilliQ water, 70% ethanol and MilliQ water and dried with nitrogen before being glued with two-component epoxy glue (Bison Kombi Snel-rapide) to a microscope slide (76 x 26 mm, thickness: 0.1mm, Menzel Gläser). After the glue has cured, the device is treated with UV/ozone at 75 Watt 100 mTorr O_2 for 5 minutes (Plasma Prep III, SPI) to remove any organic contaminants and render the surface hydrophilic.

Within 5 minutes after treating the wafers, we placed a ring of grease (Z273554, Sigma-Aldrich) on top of the treated silicon, wherein we added 100 µL of 0.25 mM 5% PIP_2 vesicle solution diluted in NaCi-buffer. After 30 minutes at room temperature, the vesicles are washed away by replacing the liquid with 300 µL of F-buffer and leaving 50 µL.

3.3 Cortex reconstitution

3.3.1 Glass-supported lipid bilayers

For the fluorescence microscopy assays, we formed a glass-supported lipid bilayer on which we added our proteins at room temperature. To do this, we sequentially added lipids and proteins to either a flow channel or a chamber. The construction of the SLB and usage of these devices are described in section 3.2.

Proteins are added sequentially to the SLB. The membrane-binding protein (septin or VCA) is added first and is incubated for 20 minutes. After incubation, the unbound proteins are removed by replacing the buffer with three times the device's volume. Next, the remaining proteins are added (actin or actin with Arp2/3) in imaging-buffer to the SLB.

3.3.2 Silicon wafer-supported lipid bilayers

For the AFM assays, we formed a silicon wafer-supported lipid bilayer on which we added septin. The formation of the silicon wafer-supported lipid bilayer is described in section 3.2.1. After formation and washing of the SLB, we added 50 µL of septin in polymerisation-buffer with 1 mM MgGTP to the SLB, for a total volume of 100 µL. Then the septin is incubated for at least 20 minutes and washed with 300 µL F-buffer, leaving 100 µL.

In some experiments, we fixed the sample with 1 wt-% glutaraldehyde (GTA) (G7651,Sigma-Aldrich). This was done by replacing 50 µL of the sample with 2 wt-% GTA in F-buffer and incubating the sample for 1 minute. Next, the sample is washed with F-buffer.

3.4 Cortex reconstitution on EM-grid-supported lipid monolayers

We produced supported lipid monolayers at room temperature by first allowing a lipid monolayer to self-assemble at the air-water interface and then transferring it onto a transmission electron microscopy grid. To image reconstituted cortices with transmission electron microscopy (TEM), we formed cortices on lipid monolayers.

We let a lipid monolayer form and use the transfer technique to deposit the monolayer with the network to an EM-grid [54, 60]. Before transferring the monolayer, we reconstituted the desired cortex by first adding the actin anchor or nucleating proteins and then actin. Finally, we negatively stain the proteins.

During this project, we have used two types of wells for lipid and protein transfer to an EM-grid. The 100 µL-wells are caps of a 0.5 mL Eppendorf tubes (0.5 mL Eppendorf Safe-Lock Tubes, Eppendorf). The 30µL-wells are wells in the Microwell Staining Mold (103, Ted Pella), which we cleaned between uses by sonicating (Branson Ultrasonic Bath, Branson) for 5 minutes in ethanol, and subsequently in MilliQ water. At room temperature, we dissolved the lipids with the desired species composition in chloroform. We used a total lipid concentration of either 0.005 mM or 0.01 mM. Next, we added 100 or 30 µL proteins in polymerisation-buffer to the well. To form the monolayer, we then usually dropped 2 µL of 0.005 mM or 0.01 mM dissolved lipid mixture on the well using a 5 µL Hamilton syringe. For each TEM images shown in chapter 4 we noted the lipid concentration, drop volume and well used in section 8.2. The well is then incubated at room temperature for at least one hour to bind the proteins to the lipid monolayer.

After one hour, an EM-grid (QF300 R1.2/R1.3 or C support Cu400) is placed with a crossover tweezer (AGT5293, Agar Scientific) on top of the well for 2 seconds. The monolayer with attached proteins will adhere to the grid [54]. For some experiments, we transferred the grid to a second well with (1 µM, 2 µM or 4 µM) pre-polymerised actin, where it incubated for 1 hour. Finally, the grids were fixed and stained by adding 3 µL of 2% uranyl acetate and blotting after 30-60 seconds with blotting paper (Qualitative filter paper,Whatman).

We used EM-grids designed for cryo-EM (QF300 R1.2/R1.3) to increase contrast. Because a monolayer can span over the holes in the carbon [54], the electron beam will only strike the lipids and proteins stained with uranyl acetate within the holes. However, the monolayers over the holes are fragile since they have no support. For this reason, we did not wash the sample before staining.

3.5 Microscopy

3.5.1 Total internal reflection microscopy

In total internal reflection fluorescence (TIRF) microscopy, the laser is directed to the coverslip above the critical angle [61]. This angle of incidence results in total internal reflection, where the propagating wave is reflected entirely out of the sample. As a result, only an evanescent wave penetrates the sample, which decays within around 100 nm above the sample-coverslip interface. This evanescent wave can excite fluorophores, resulting in a fluorescent signal that can be captured and filtered by the microscope. TIRF microscopy will only excite fluorophores within 100 nm from the surface, which results in less out-of-focus fluorescent signal, reducing the signal-to-noise ratio. To perform TIRF microscopy, we need to include fluorescent tags of our protein of interest.

We used two TIRF microscopes available in our lab. The first setup (TIRF-1) consists of Nikon Eclipse Ti inverted microscope with an Ilias^2 system (Roper Scientific). The Ilias^2 system allows for dual azimuthal spinning TIRF illumination. During this project, we used a 488 nm, 561 nm, and 642 nm laser. We also used the ZT405/488/561/640rpc dichroic mirror. The TIRF-1 uses a Nikon CFI Plan Apochromat 100XH NA1.45 TIRF oil objective and two Evolve 512 EMCCD camera's (Photometrics), which allows for simultaneous dual-acquisition. However, before the light reaches the camera, it passes through a 525/50 nm or a 609/54 emission filter and is magnified by an additional magnifying lens. The final pixels size for the TIRF-1 is 107 nm/pixel. The sample is kept in focus with the Nikon Perfect Focus system and uses a Nikon

motorised stage. MetaMorph 7.8.8.0 (Molecular Device) was used to control the hardware.

The second setup (TIRF-2) consists of a Nikon Eclipse Ti inverted microscope with an Ilias^2 system (GATACA SYSTEMS). The Ilias^2 system allows for dual TIRF illumination. During this project, we used a 488 nm, 561 nm and 637 nm laser. The TIRF-2 uses a CFI Apochromat TIRF 100XC oil objective and an EAndor iXon Ultra 888 camera. However, before the light reaches the camera, it passes through the ET525/50m, ET609/34m, and ET700/75m (Chroma) emission filter and is magnified by an additional magnifying lens. The final pixels size for the TIRF-1 is 129 nm/pixel. The sample is kept in focus with the Nikon Perfect Focus system and uses a Nikon motorised stage. MetaMorph 7.8.8.0 (Molecular Device) was used to control the hardware.

FRAP assay
Both TIRF microscopes are equipped with fluorescence recovery after photobleaching (FRAP) hardware. This hardware allows the microscopes to expose a region (FRAP region) to high laser intensity. When performing a FRAP assay on an SLB, the fluorophore in the labelled lipids in the FRAP region will photobleach. Due to the diffusion of lipids, unbleached lipids will move into the bleached region while bleached lipids will move out. This diffusion will lead to a recovery of the fluorescence in the area. Furthermore, when FRAP is performed on membrane-bound proteins, recovery of the fluorescence signal indicates whether the protein binding is dynamic. We performed FRAP experiments by time-lapse acquisition at 0.6 seconds per frame, and approximately after 5 seconds, a manually selected region was exposed to 100% laser intensity. We used the FRAP experiments as a qualitative test for the SLB fluidity and septin binding.

3.5.2 Atomic force microscope

Atomic force microscopy is a technique where you probe the sample with a small tip. This tip is attached to a cantilever that can control and measure the tip position. The microscope controls the cantilever movements depending on the imaging mode. We imaged with a Bruker AFM using mainly Quantitative Imaging mode (QI™mode) for imaging for our project but have also used AC mode. QI™-mode is an imaging mode that makes a force-distance curve for each pixel and uses the force as feedback. Amplitude Controlled mode (AC mode) is an imaging mode that oscillates the cantilever at a fixed amplitude by changing the piezo height.

The AFM setup for image acquisition consisted of a Nanowizard 4 XP Bioscience (Bruker) with a silicon cantilever (ScanAsyst-Fluid+; Bruker) using the JPK Fast Scanner cantilever holder (Bruker). The cantilever we used has a nominal spring constant of 0.7 N/m with a pyramidally shaped tip with a nominal radius of 2 nm. Most images were acquired using QI™-mode, taking images of 512×512px at a scan rate of 3-5ms/pixel with a typical maximum force of 1.5 nN and a distance covered by the z-piezo of 50-100 nm. The images of septin on mica-supported lipid bilayers were acquired using AC-mode, taking images of 512×512px at a scan rate of 0.8lines/s with a target amplitude around 20 nm, a relative setpoint around 50 %, and a gain above 120.

3.5.3 Negative stain transmission electron microscopy

Transmission electron microscopy is a technique where a beam of electrons is transmitted through your sample. We increase the contrast of our specimen using uranyl acetate, a negative stain, which embeds proteins bound to the EM grid with the heavy metal uranium, which strongly scatters electrons. We acquired electron microscope images with the JEM-1400Plus transmission electron microscope (JEOL) equipped with a CCD camera operated at 120kV.

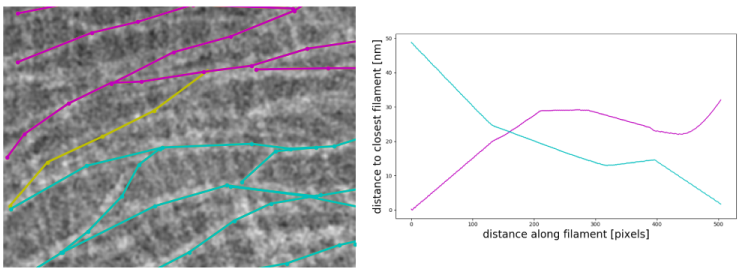

Figure 6: **Example of minimum distance calculation between manually detected filaments.** TEM image shows an example of manually detected paired septin filaments. The graph next to the image shows the distance along the yellow line between its upper (magenta) and lower (cyan) neighbours.

3.6 Image analysis

3.6.1 EM images

We manually detected filaments for the septin hexamers incubated on 5% PIP_2 lipid monolayers. We did this by tracing the filament by eye with a linear spline. Unfortunately, we only could trace paired filaments, which showed clear contrast. We noticed most detected filaments formed an array. We manually sorted the filaments part of this array. Next, we calculated the minimum distance along each filament in the array to the filaments above and below it (an example is shown in figure 6). Finally, when a filament ends and a neighbouring filament continues, we will measure the distance between a single point and the rest of the continued filament. We manually filtered these edge cases. The code for finding the minimum distance between filaments can be found at `https://github.com/djimderidder/2021imageAnalysisMEP`. For the angle measurements for septin cross-hatching meshworks and actin filaments polymerised by Arp2/3, we used FIJI to calculate the acute angle between crossing filaments.

3.6.2 AFM images

The AFM images were first processed using Gwyddion [62]. We first corrected for sample tilt by second-order flattening the images. Next, we corrected for scan line artefacts by aligning the rows and correcting for scars. Finally, I exported the processed AFM data to an Excel file and performed the additional analysis with custom written code in Python, which can be found at `https://github.com/djimderidder/2021imageAnalysisMEP`.

To analyse the height profiles, we did a non-linear least-squares fit (SciPy package) of a bimodal distribution to the histogram of the height data. To analyse the bundles' width analysis, we calculated the minimum distance between the bundles' centre and contours. The centre was estimated by performing a skeleton operation (scikit-image package) on an Otsu thresholded binary image. At the same time, the contour was found by a marching squares algorithm (scikit-image package).

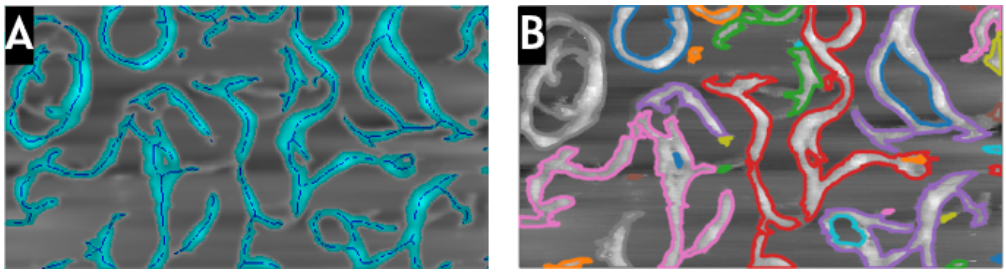

Figure 7: **Images analysis for bundle width measurements.** Grayscale images show an example of a septin bundle AFM image. (A) Results from skeleton detection, shown with blue overlay. The cyan overlay shows the binary image after Otsu thresholding.(B) Results after

4 Results

During this research, we aim to gain an understanding of human septin organisation on model membranes and investigate the recruitment of actin by membrane-bound septin. To this end, we imaged minimal reconstituted cortices on supported lipid layers with AFM and TEM. In this chapter, we will show and review the results.

4.1 Membrane-bound septin network

Septin is known to bind to actin [27], and to negatively charged lipids [63, 64]. In the following section, we want to reveal the structure formed by human septin on membranes. To this end, we reconstituted septin networks both on supported lipid monolayers and on supported lipid bilayers to image by EM and AFM, respectively.

4.1.1 Septin cortex reconstitution on glass-supported lipid bilayers

Before discussing the high-resolution techniques, we tested human septins' affinity to negatively charged membranes with TIRF microscopy. As described in section 3.2 and section 3.3.1, we formed an SLB on glass and wash the sample with F-buffer before adding septin. Our group has previously shown that flat lipid membranes recruit fly septins using this methodology [25]. We co-polymerised 100 nM human septin octamers or hexamers with 10% GFP-labeled septin in imaging-buffer with 1 mM MgGTP on a 5% PIP_2 SLB (5:94.7:0.3 PIP_2: DOPC : cy5-PE). We observed an intensity signal that appears homogeneous but somewhat grainy for both septin octamers and hexamers. We observed a uniform intensity with bright dots for the lipid membrane, likely remaining intact SUVs. An example for the octamers on a 5% PIP_2 SLB is shown in figure 8, while the data for the hexamers are not shown. Human septin has previously been shown to form bundles in the absence of lipids [56]. The homogeneous signal suggests septin covers the SLB, showing septin preference to interact with the membrane over bundling. This observation is in accordance with the high affinity to negatively charged lipids of Fly septin incubated on an SLB [25].

To verify the fluidity of the SLB, we performed a FRAP assay (section 3.5.1). For the lipid membrane, we observed the bleached region (dark round region) shrinks after laser exposure and, after approximately a minute, recovers most of its intensity. In figure 8, an example of septin octamers on a 5% PIP_2 SLB is given, while the data for the hexamers are not shown. This fluorescence recovery proves we still have a fluid membrane in the presence of septin. However, the FRAP region will not completely recover its original intensity because of an immobile fraction of lipids in the SLB. There will also be some photobleaching during imaging, contributing to incomplete fluorescence recovery (dashed region in figure 8). We also performed a FRAP experiment on the hexamers and octamers layers to investigate if the SLB bound septin is dynamic (figure 8B). We observed no fluorescence signal recovery, indicating that septin is stably anchored to the membrane, and there is no dynamic exchange of septin.

4.1.2 Electron microscopy imaging of septins on lipid monolayers

The TIRF microscopy results show that septin binds to a flat membrane layer with negatively charged lipids and forms a static structure. However, due to the resolution constraints of fluorescence microscopy, we can not resolve individual septin filaments. Therefore, to observe the morphology of the septin layer on lipid layers, we turned to two high-resolution methods, TEM and AFM. In this section, we will discuss the results from TEM.

Yeast and fly septins bound to lipid monolayers have already been imaged with TEM [9, 23]. Therefore, we followed a similar protocol, described in section 3.4, where we transferred a lipid monolayer incubated with septin from a well to an EM grid and negatively stained the protein with 2% uranyl acetate.

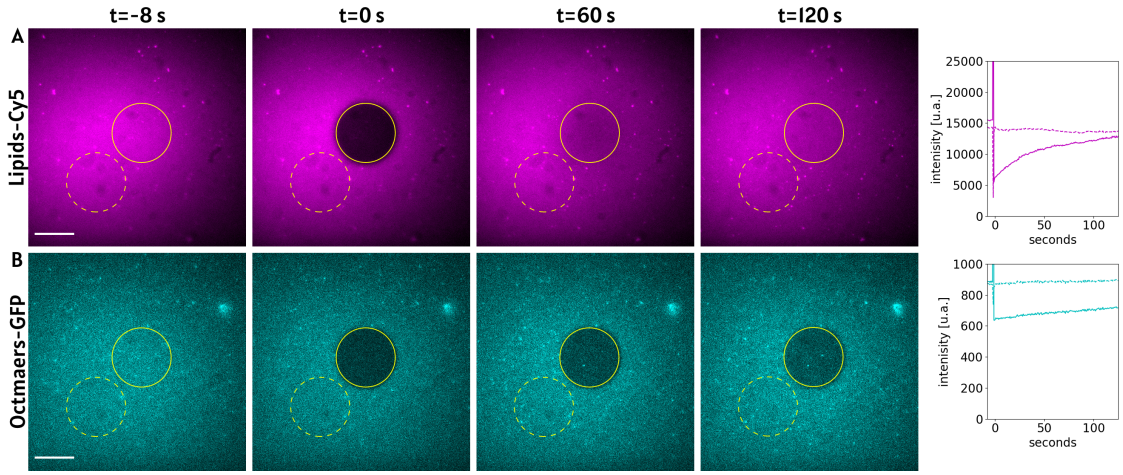

Figure 8: **Septin octamer forms stable layer on fluid SLB.** TIRF images (acquired from TIRF-1) of 100nM octamers on 5% PIP_2 SLB assembled in a chamber. After photobleaching, the SLB recovered after two minutes (A), while the octamer layer did not recover (B). The graphs next to the images are the mean intensity over time within the depicted areas on each image. Scale bar: 10 µm

We observed that septin hexamers self-assembled into various qualitatively distinct structures even within one condition. Figure 9 shows an overview of these structures found when imaging 50 nM septin hexamers incubated on a 5% PIP_2 (5:95 PIP_2: DOPC) lipid monolayer. We found that hexamers can form dense meshworks of locally aligned filaments, as shown in figure 9A, B, C. The dense networks are consistent with the homogenous septin layer we observed in TIRF microscopy since a high-density meshwork could produce a homogenous fluorescence signal. However, we also occasionally found bundles (figure 9D), individual filaments (figure 9E) or individual hexamers (figure 9F). The individual filaments and hexamers are 4 nm in width (yellow arrows in figure 9) corresponding to septins' width [16]. And the individual hexamers are recognised by their length of 24 nm [16].

To increase contrast, we imaged the septin on lipid monolayers on holey carbon grids. Figure 9 shows septin organisation over the holes. In section 8.3 we show uranyl acetate can form thin layers over the holey carbon without lipids. This observation could explain why we find variety in septin structures since we might image septin over holes with no lipids. Further experiments could try to detect the absence of the monolayer in these regions. One way would be to use confocal imaging, which has been used to detect bilayers on EM grids [52].

We sorted the data for meshworks of septin with good contrast to investigate the septin organisation. The high resolution from EM allowed us to see single filaments (4 nm in width) aligning next to each other (figure 9A). However, we also observed threads of approximately 10 nm in width (black arrows in figure 9) in about two-thirds of the sorted meshworks. Since septin hexamers have a width of 4 nm [16], these threads could be paired filaments, previously observed in yeast [65], fly and human septin [25]. A closer inspection reveals that these paired filaments can split, shown with the white arrow in figure 9B. We also observe the septin meshworks to show a cross-hatching pattern of closely spaced parallel filaments at a certain angle. This cross-hatching patterned meshwork has previously also been observed for yeast septin octamers on curved membranes [8].

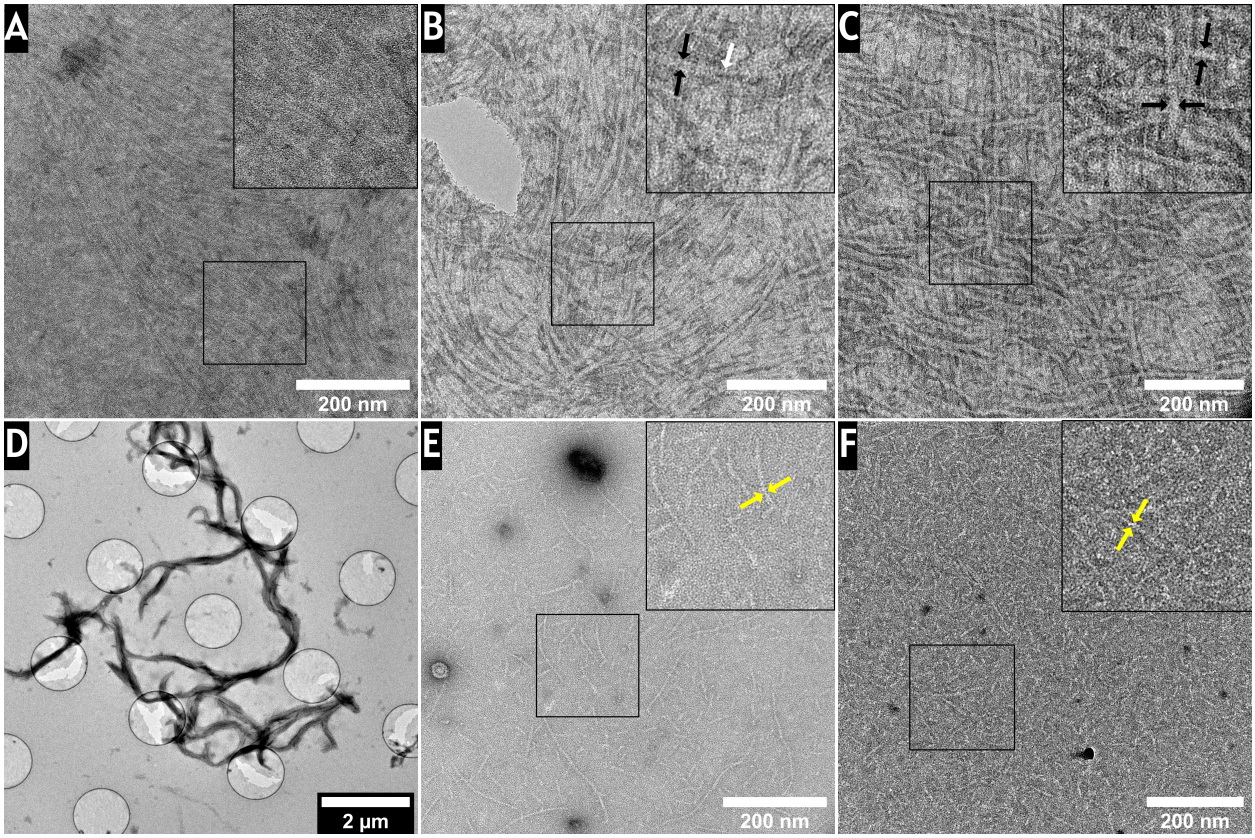

Figure 9: **We find qualitatively distinct structures for human septin hexamers on monolayers.** The images were acquired using negative stain TEM of 50 nM hexamers incubated with a 5% PIP_2 lipid monolayer. We find meshworks of septin filaments (A). In addition, we can observe paired filaments within these meshworks (B, C). The white arrow shows paired filaments splitting. We also find septin bundles (D), single filaments (E) and single hexamers (recognisable by their 24 nm length) (F). The black and yellow arrows indicate examples of filaments, for which we measured widths of 10 nm or 4nm, respectively. Zoom ins on the septin structure are shown in the insets of the figures.

We next investigated the structural properties of the observed meshworks more closely. For this, we manually detect the hexamer paired filaments inside the dense networks on 5% PIP_2 (5:95 PIP_2: DOPC) lipid monolayer. Because single filaments were difficult to detect and we had insufficient data for octamers, we only analysed paired hexamer filaments. Figure 10A shows an example of the detected paired filaments. Note that we found most of the paired filaments aligned in a similar direction. Occasionally, however, we find paired filament perpendicular to this main direction (figure 10B). This perpendicular direction coincides with the main direction of single filaments inside the image.

Measuring the distance between parallel paired filaments for nine images using the methodology described in section 3.6 we find a broad peak from 14-29 nm with a tail reaching up to 60 nm (figure 10A). We also see a peak at 0 nm. The peak at 0 nm is caused by the merging of filaments. The measurement showed an average interval distance between the paired filaments of 21.42 $\pm$ 10.41, comparable to the length of a single hexamer of 24 nm [16]. Fly and yeast septin have also shown arrays with similar interval distance [23, 25], which were speculated to be caused by septin bridges between filaments. We did not find these bridges. However, we found single filaments perpendicular to the bundled arrays. The spacing of the paired filaments could be explained by paired filaments interacting with the hexamers inside the single filaments. This hypothesis is consistent with the observed gaps in the paired filaments arrays (figure 10A) since the paired filament array could have skipped hexamers inside the single filaments.

We only manually detected a few paired filaments perpendicular to the detected paired filaments array (figure 10B). We manually measured N=182 angles of filaments between the perpendicular filaments arrays to be 85.02 nm ± 13.21 nm (figure 10B). We could not track the single filaments by eye, meaning the second array of parallel filaments could mainly consist of single filaments. To confirm this, we manually measured the width of a few single filaments to be 4 nm (indicating by the magenta arrows in figure 10A). Next, we wanted to see if we could quantify the cross-hatching patterns of the septin meshworks by looking for a bimodal distribution of the image gradient orientation. We estimated the gradient orientation with the Sobel operator but, unfortunately, did not find a clear bimodal distribution (figure 10C).

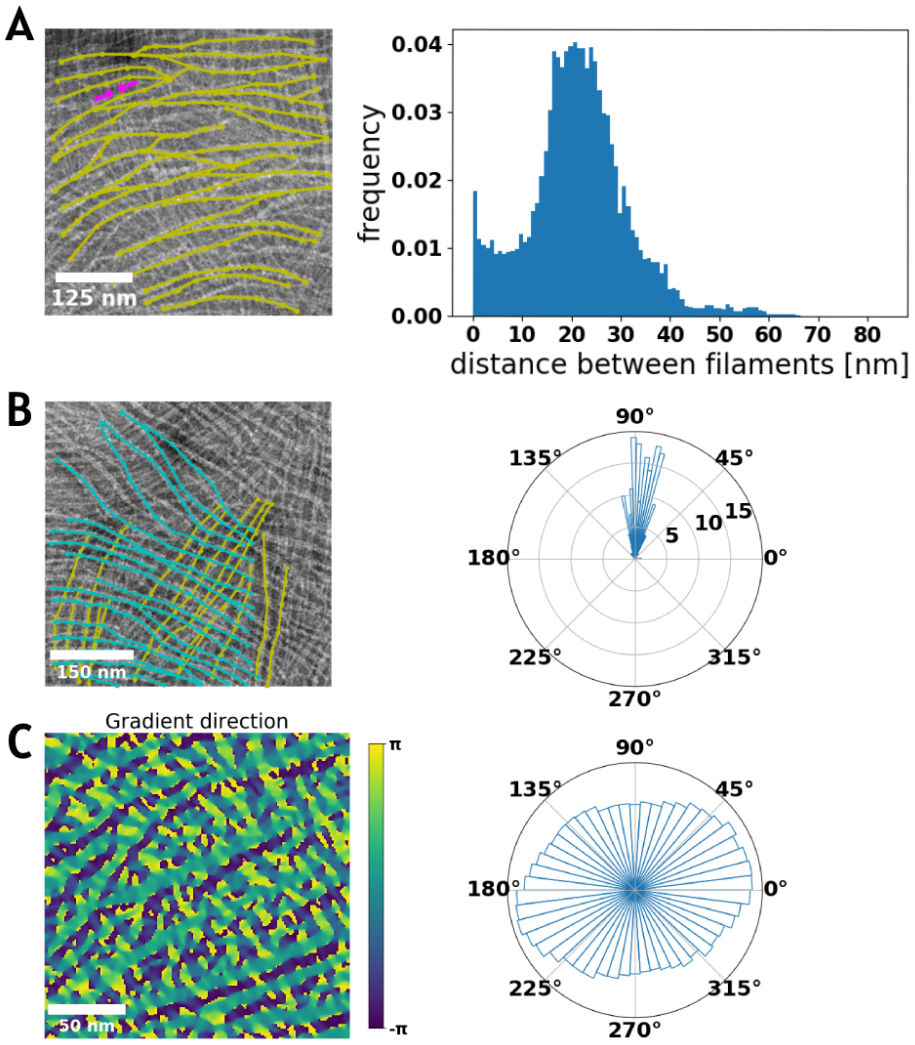

Figure 10: **Cross-hatching patterned meshworks consist of an array of paired filaments.** The figures show the results of the image analysis of septin filament meshworks for N=9 images of 50 nM hexamers incubated on 5% PIP_2 monolayer acquired with TEM. (A) The histogram (right) (# bins= 100) shows the measured distance between neighbouring detected paired filaments. An example of the detected paired filament (in yellow) is superposed on the original image (left). The magenta arrows indicate an example of filament with a width of 4 nm we were unable to manually track. (B) The circular histogram (right) (# bins= 50) shows the measured angle between intersecting detected paired filaments. An example of the detected intersecting paired filaments (yellow and cyan) is superposed on the original images (left). (C) The gradient orientation of one of the analysed images, with the distribution shown in the circular histogram (right) (# bins= 50).

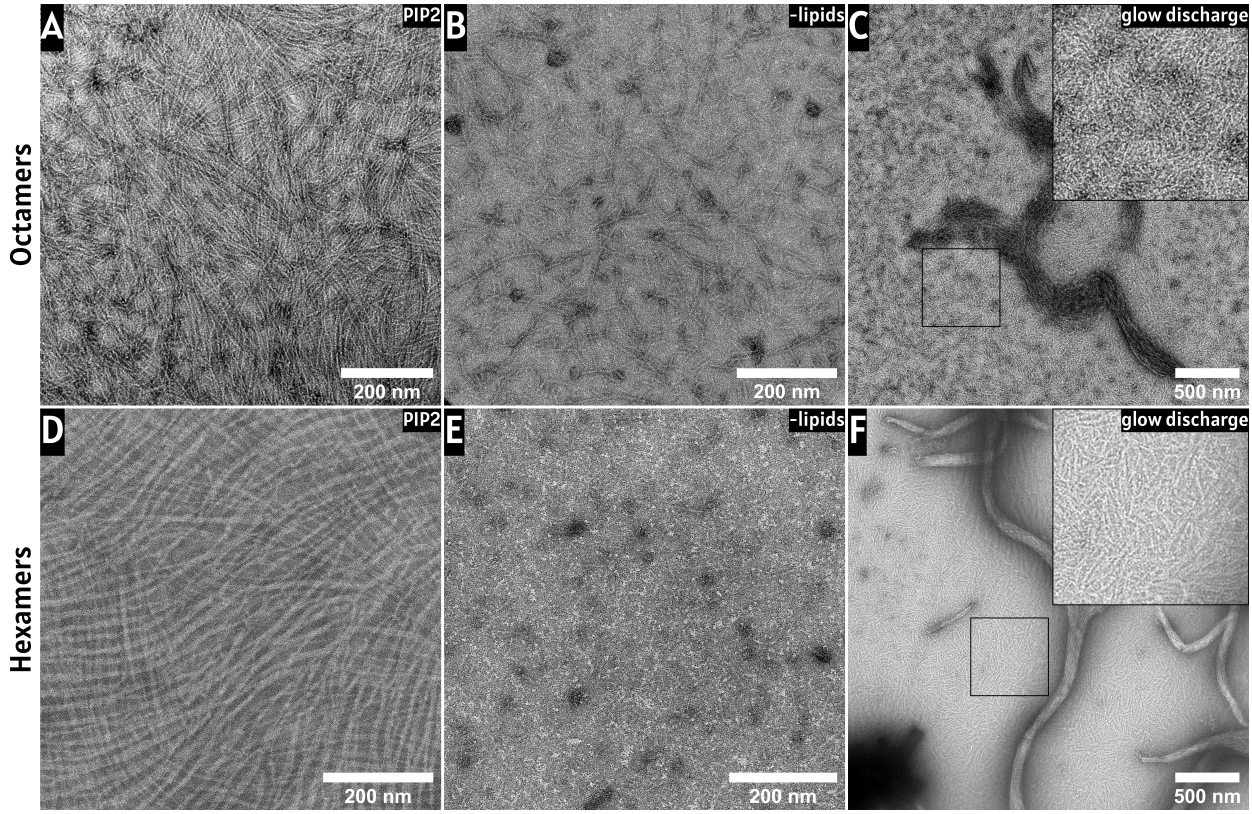

Figure 11: **Both septin hexamers and octamers form meshworks on 5% PIP_2 monolayers.** The images are acquired using negative stain TEM of septin octamers and hexamers incubated on a 5% PIP_2 lipid monolayer (A, D), carbon (B, E) and glow discharged carbon (C, F). (A, D) Septin octamers and hexamers organise into an aligned meshwork of filaments when 50 nM septin is incubated with a lipid monolayer. (B, E) We observe less surface binding of septin octamers and hexamers and fewer filaments when 50 nM septin is incubated on the carbon grid compared to on a lipid monolayer. (C, F) Incubating 300 nM septin on a glow discharged carbon grid increases the density of surface-bound septin compared to a non-charged grid. Zoom ins on the septin-coated structure are shown in the insets of the figures, which shows a few septins organising into filaments.

To see the monolayers' influence on the septin organisation, we imaged hexamers without an underlying lipid monolayer binding to EM-grids. We expected septin not to interact with the carbon and indeed found fewer hexamers without the 5% PIP_2 monolayer (figure 11E). However, we might still find septin binding to the carbon since we did not wash the sample before staining. To promote septin carbon binding, we incubated septin on a glow discharged EM-grid. We found that the septin density indeed increases (inset of figure 11F). Note that the septin forms fewer and shorter filaments without a lipid monolayer, with most of the septin showing as hexamers recognisable by their 24 nm length [16]. In the absence of a lipid monolayer, the septin also shows no alignment with other septins, implying lipids promote filament organisation and are necessary for the alignment of the septin network.

To see if the septin structure in the presence of a lipid monolayer is the same for hexamers and octamers, we performed the same experiment for octamers. Similar to the hexamers, we observed fewer septin for the octamers on non-charged and glow discharged carbon (figure 11B,C) compared to filaments on 5% PIP_2 monolayers (figure 11A). We again noticed that only the octamer filaments on 5% PIP_2 lipid monolayers showed two arrays of long filaments perpendicular to each other, implying the octamers show similar organisation and cross-hatching on lipid monolayers as hexamers.

Finally, we found septin bundles when we incubated 300 nM of septin on glow discharged grids (11C, F). Human septin has previously been shown to self organise into bundles in solution for a concentration of 200 nM [56]. We did not image septin on monolayers at a concentration above 50 nM. In the future, septin bundle organisation on lipid monolayers for higher concentration can be explored.

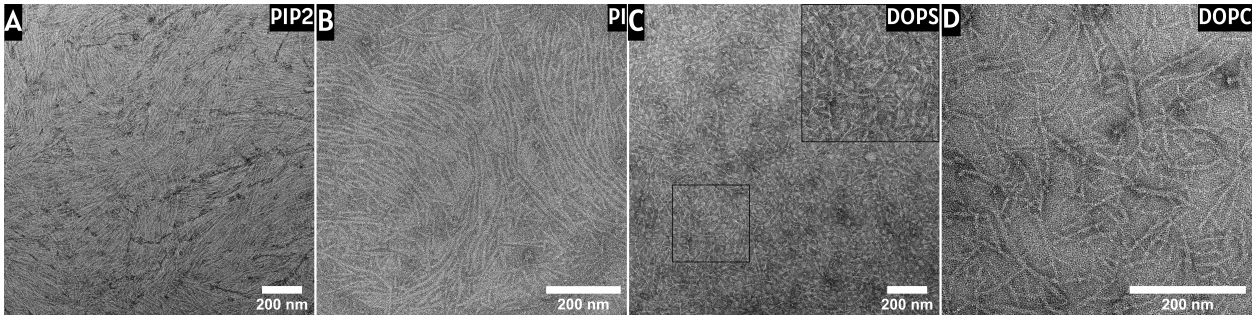

Figure 12: **Septin octamers binds to negatively charged lipid monolayers**; The images were acquired using negative stain TEM of 50 nM octamers incubated with lipid monolayer with different lipid compositions. (A-C) Septin organises into an aligned meshwork of filaments on a monolayer containing 5 % PIP_2, 6 % PI or 20 % DOPS, respectively. (D) In the absence of negatively charged lipids, septin forms fewer filaments, showing no clear alignment.

Septins have been shown to bind to different lipid bilayer compositions [25, 66, 67]. Therefore, we tested whether human septins also display this behaviour by allowing septin octamers to self-assemble on lipid monolayers of different compositions (5:95 PIP_2: DOPC, 6:94 PI : DOPC, 2:8 DOPS : DOPC, DOPC), shown in figure 12. DOPC is a neutral lipid, while DOPS PIP_2 and PI are anionic lipids. At neutral pH, DOPS and PI have a net charge of -1, while PIP_2 has a net charge of -4 [13]. We found that septin forms cross-hatched structured meshworks of aligned filaments on 5% PIP_2 and 6% PI monolayers. On 20% DOPS monolayers, we observed less dense septin filaments where in some regions, we found cross-hatched patterned meshworks. We do note we had fewer images with good contrast for septin on DOPS monolayers. On DOPC monolayers, we find mainly octamers and a few short septin filaments that did not show any alignment, similar to the structure found in the absence of a lipid monolayer. These results suggest negatively charged lipids (PIP_2, DOPS and PI) are necessary for septin binding. These findings are consistent with earlier studies of Fly septins, which have been shown to bind to DOPS and PIP_2 monolayers and not to DOPC monolayers [25]. Furthermore, we also incubated 50 nM human hexamers on a 6% PI monolayer (shown figure 25A, B) and found meshworks of aligned filaments.

Previous studies showed human septin binding to PIP_2 [67] and DOPS [25], but we did not find studies for human septin binding to PI. However, yeast septin has been shown to bind to PI lipids [66]. Here we showed human septin octamers and hexamers are also able to bind to PI lipids. We did not study the difference in septin organisation for different lipid compositions since we did not have enough images to do a thorough analysis.

4.1.3 Atomic force microscopy imaging of septins on lipid bilayers

The second high-resolution method we will discuss to study the structure of septin on supported lipid layers is AFM. In contrast to TEM, which is performed in an ultra-high vacuum, AFM allows probing of the surface in an aqueous environment. In addition, while generally, AFM has an order of magnitude lower lateral resolution [68, 69], it can also image non-fixed samples. As a result, AFM allows imaging in the liquid phase at the expense of resolution. Furthermore, the ability of AFM to image in an aqueous environment allows imaging of reconstituted systems on SLBs [70, 71].

We performed AFM imaging on septin networks reconstituted on lipid bilayers rather than monolayers, as these more closely match the plasma membrane. We used a similar protocol as the one previously reported for studying fly septins on SLB with AFM [25], described in section 3.3.2. The two substrates we tried for SLB formation are mica and silicon wafers. While mica allows for simultaneous fluorescence imaging of the same sample, we were not able to consistently form fluid SLBs on mica (see section 8.1). For this reason, we will only discuss septin networks on silicon wafer-supported lipid bilayers.

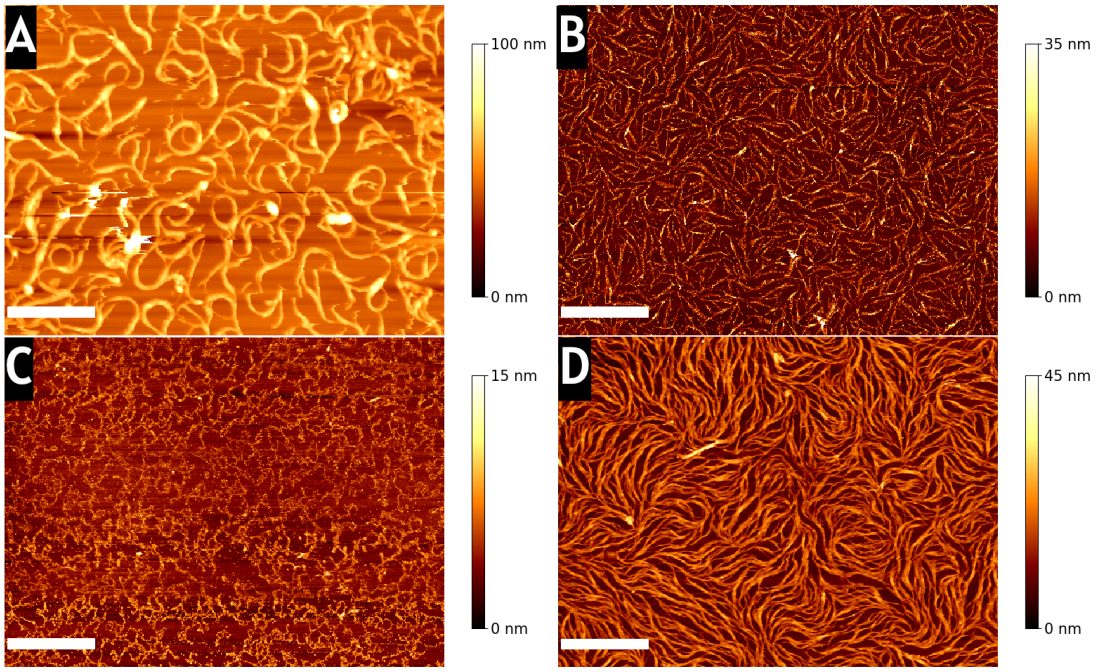

Figure 13: **AFM image of septin hexamers organisation on a 5% PIP_2 SLB.** Images show examples of the four different morphologies we find for 120 nM septin organising on a 5% PIP_2 SLB, acquired using AFM. The bottom two images are imaged after fixation with 1% GTA. Scale bars: 2 µm. Colour bars on the right of the images display the height scale.

As described in section 3.2.1, we incubated 120 nM septin hexamers on a 5% PIP_2 (5:95 PIP_2: DOPC) SLB for 20 minutes. We found different morphologies for different samples with the same conditions, shown in figure 13. In general, we noticed that septin organises into bundles that form a network. The results range from a less dense network of curvy bundles (figure 13A) to a more dense network of locally aligned bundles (figure 13C and 13D). We also found short clusters of septin (figure 13B), which have a significantly different morphology than the other networks we found. These clusters of septin might correspond to the denaturation of septin filaments. For this reason, we will only analyse the network morphologies of figure 13A, B, D, which we will refer to as sparse, medium-density and dense bundle networks, respectively.

To investigate whether the tip movement introduced artefacts in our imaging, we compared non-fixed samples with the fixed AFM data. We only observed the dense bundle network with fixation and the sparse bundle network without fixation. However, we found medium-density bundle networks in both fixed and unfixed samples (figure 14). This observation indicates the fixation did not change the morphology significantly. However, fixation did help with imaging the septin networks since we were able to obtain images more easily. This could be because fixation reduced tip disruption by septin. As a result, we did not analyse the unfixed sample of the medium-density bundle network morphology.

First, we will compare the fixed sample morphologies (the medium-density and dense bundle networks). The height of the AFM data showed a bimodal distribution for both types of networks (figure 15A, B). We assumed the two modes of the distribution correspond to the membrane and the septin, respectively. By fitting a sum of two Gaussians (figure 15A,B) we find the average height from the surface to be 5.66 nm±0.88 nm (N=6) for the medium-density networks and 9.55 nm±0.22 nm (N=3) for the dense networks (figure 15D). The fitting is described in section 3.6.2. The height of the medium-density bundle networks is close to septins' width of 4 nm [16], while the height of the dense bundle networks is almost double. This observation indicates the bundles vertically consist of one hexamer for the medium-density networks and two hexamers for the dense networks. From the fitted Gaussian, we can also determine the fractional coverage of the septins by determining the area under the peak. We find the septins' fractional coverage to be 47% ± 9% (N=6) for the medium-density networks and 71% ± 2% (N=3) for the dense network (figure 15D).

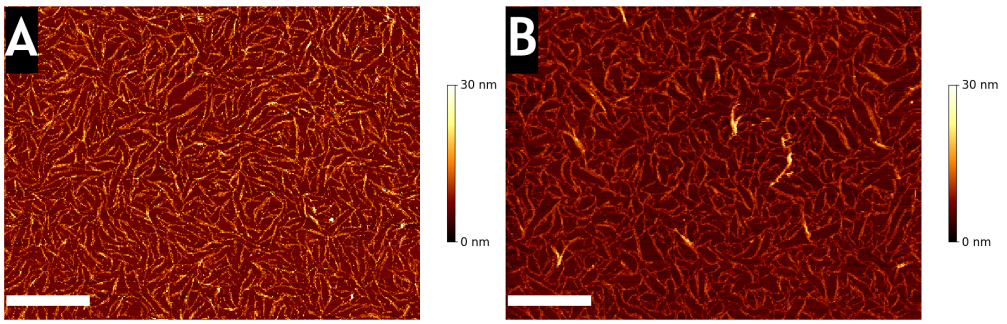

Figure 14: **We find the medium-density bundle networks for both fixed and non-fixed septin layers.** AFM images show 120 nM septin hexamers on a 5% PIP_2 SLB, acquired with AFM. (A) Shows an example of medium-density bundle networks fixed with 1% GTA. (B) Shows an example of medium-density bundle networks not fixed with GTA. Scale bars: 2 µm. Colour bars on the right of the images display the height scale.

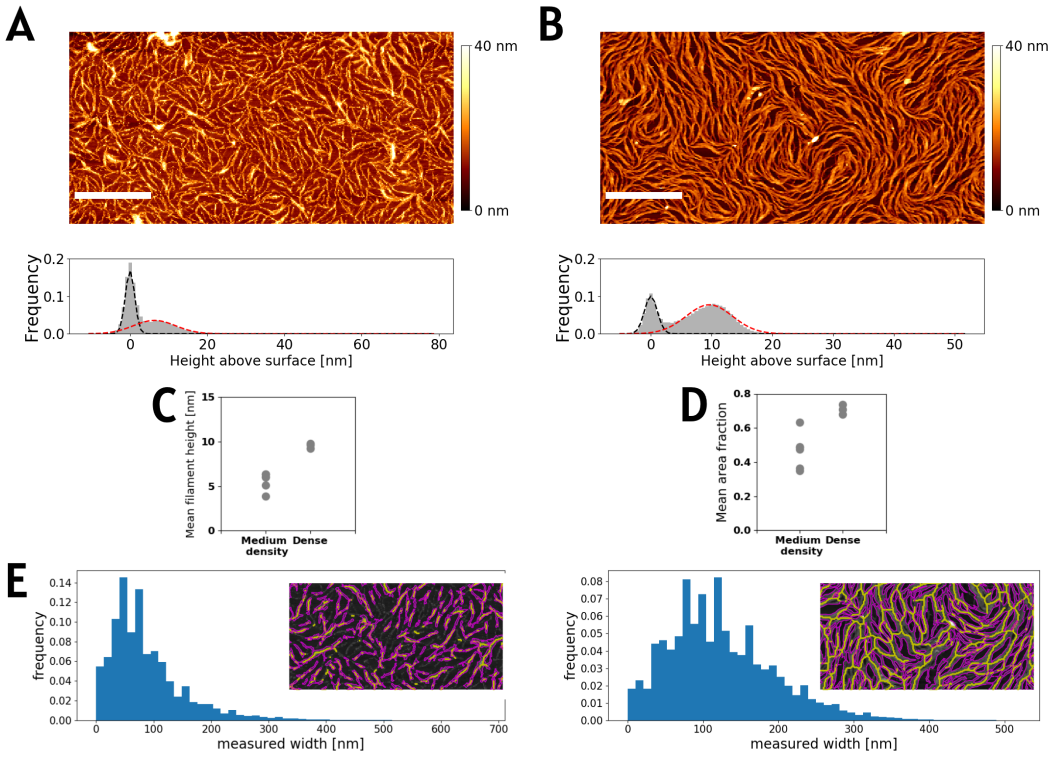

Figure 15: **The dense bundle networks have broader bundles with twice the heights compared to the medium-density bundle networks.** The AFM images show 120 nM septin hexamers on a 5% PIP_2 SLB fixed with 1% GTA. (A, B) The histogram shows the height distribution (above the surface) of the AFM images above. We fitted a bimodal function to the height distribution, where the first peak corresponds to the SLB while the second peak corresponds to the septin. We correct the height distribution in the histogram by setting the mean of the first peak to zero. (C) The mean of the septin height distribution above the surface for the dense (N=3) and medium-density bundle networks (N=6). (D) The area fraction covered by septin for the medium-density (N=6) and dense (N=3) bundle networks (N=6). (E) Shows a histogram for the estimated width of the bundles. This width is measured by finding the minimum distance between the skeleton and edges of the bundles for the medium-density (N=6) and dense (N=3) bundle networks. Scale bars: 2 µm. Colour bars on the right of the images display the height scale.

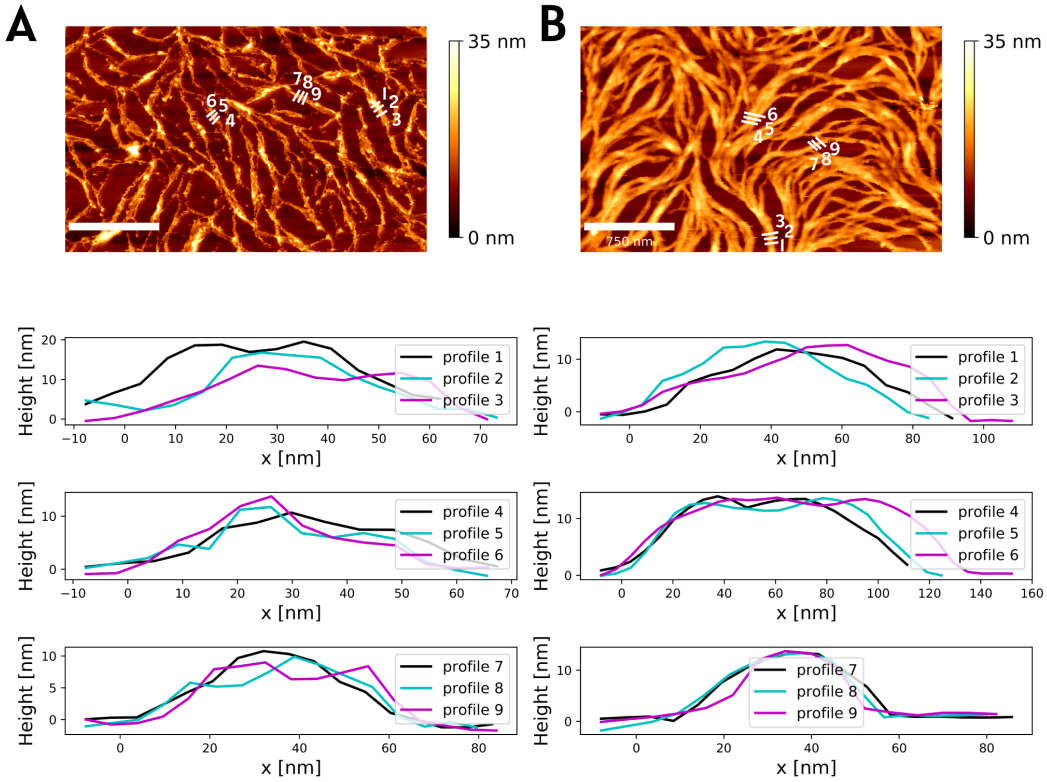

Figure 16: **Line profiles show height fluctuation along the bundle short-axis for the dense bundle networks.** The AFM images show 120 nM septin hexamers on a 5% PIP_2 SLB fixed with 1% GTA. The profile plots below show the height profiles along the numbered lines drawn on the AFM images. The height in the profile plot is corrected to show the height of the membrane surface. Scale bars: 750 nm. Colour bars on the right of the images display the height scale.

Next, we analysed the width of the bundles for the dense and medium-density bundle networks, using the methodology described in section 3.6.2. The histogram in figure 15E shows the distribution of the width measurements for the N=6 images for the medium-density networks and N=3 for the dense networks. We measured an average width of 88.05 ±67.09 for the bundles in the medium-density bundle networks and 124.05 ±70.53 for the dense bundle networks. Comparing these distributions, we find that the dense bundle network consists of broader bundles than the medium-density bundle networks.

Finally, we investigated single bundles within the dense and medium-density bundle networks. Fixation allowed for AFM imaging at higher resolutions, caused by reduced tip disruption of septin. We looked at the height modulation of individual bundles in the medium-density and dense bundle networks (figure 16). We find the height for both types of networks to be relatively consistent at 10 nm above the SLB. However, we only observe height modulation within the bundles in the direction of the bundle's short-axis for bundles in the dense bundle networks. This height modulation is caused by the more merging and splitting of bundles in the dense bundle network compared to the medium-density bundle network. However, we still did not have a good enough resolution to distinguish the merging or splitting bundles from the height profile along the bundles' short axis.

We found both medium-density and dense bundle networks when we fixed 50 nM hexamers on a 5 % PIP_2 SLB with 1% GTA. The bundles in the dense networks are thicker bundles that vertically consist of two hexamers, while the bundles in the medium-density networks vertically consist of one hexamer. The dense network also consists of more merging bundles and shows more bundle curvature than the medium-density network. It would be interesting to explore the difference in bundle networks for the two morphologies. For instance, the bilayer could influence the bundle network formation since we did not verify the fluidity of the SLB. We also note that the width measurement (and fractional coverage) are overestimated caused by the tip convolution effect. It would be interesting to measure the width after deconvolution to see if the medium dense networks actually show bundles.

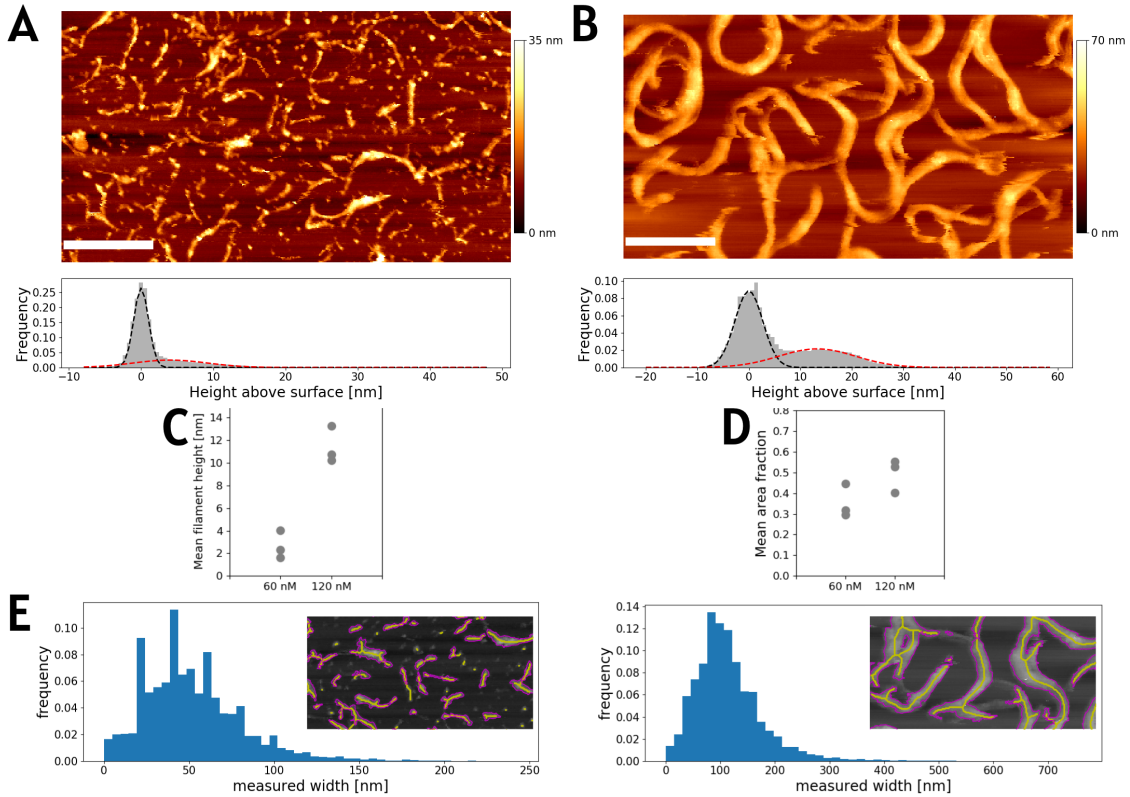

Figure 17: **Thicker bundles are observed for increased septin concentration.** The AFM images show 60 nM (A) and 120 nM (B) septin hexamers on a 5% PIP_2 SLB. The histogram below the images shows the height distribution (above the surface) of the AFM images. We fitted a bimodal function to the height distribution, where the first peak corresponds to the SLB while the second peak corresponds to the septin. We correct the height distribution by setting the mean of the first peak to zero. (C) Shows a histogram for the estimated width of the bundles. This width is measured by finding the minimum distance between the skeleton and the edges of the bundles. Scale bar: 1 µm. Colour bars on the right of the images display the height scale.

Next, we wanted to study the dependency of the bundle arrangement on septin concentration. We incubated 60 nM of hexamers on a 5% PIP_2 SLB without fixation. Septin incubated at 60 nM formed single bundles (figure 17A)), similar to the sparse bundle networks for 120 nM septin (figure 17B). The bundles for the 60 nM, however, seem to be shorter and less broad than for 120 nM.

To quantify the change of the bundle organisation with septins' concentration, we compared the 60 nM septin incubation to the 120 nM sparse bundle networks using the analysis described in section 3.6. From the height distribution fit (figure 17A, B), we found the average height of septin from the membrane to increase from 2.66 nm ± 1.01 nm (N=3) for 60 nM to 11.43 nm ± 1.31 nm (N=3) for 120 nM (figure]reffig:409C). Note that the average height for 60 nM is below the width of septin hexamers because the height distribution of the septin significantly overlaps with the height distribution on the lipid membrane. Manual height measurements of the septin bundles showed the septin is approximately 4 nm above the lipid membrane. We found the fractional coverage also increases from 35 % ± 7 % (N=3) for 60 nM to 49% ± 6 % (N=3) for 120 nM (figure]reffig:409D). We observe a peak around 50 nm for the width analysis for 60 nM hexamers and 100 nm for 120 nM hexamers (figure 17E). We measured an average width of 51.75 nm ± 28.95 nm (N=3) for 60 nM hexamers and 113.95 nm ± 62.70 nm (N=3) for 120 nM hexamers. We speculate that for the 120 nM septin, the broad peak distribution may correspond with the tapering of the bundle. In comparison, for the 60 nM septin, the broad distribution might be caused by the variety of different septin bundles.

Our analysis revealed increased septin concentration results in thicker bundles. Furthermore, the manual measured height for 60 nM is comparable to the average width of septin. And while we measured an average bundle width of 50 nm, we did not correct for the tip convolution effect of AFM. These observations could mean that the septin we observed for 60 nM might not be bundled filaments, which would indicate a

concentration limit for which septins do not bundle. In the case of fly septin hexamers, bundles have already been observed on SLBs at a concentration of 24 nM [9]. Deconvolution with the tip profile might reveal the width of the septin to be closer to paired filaments for 60 nM septins on an SLB.

To confirm that the bundle we observed are on a fluid SLB, we need to detect the SLB. For the glass-supported lipid bilayers, we could use a FRAP assay. Unfortunately, we can not perform this assay on silicon wafers since our microscopes need a transparent substrate. Therefore, to see the bilayer influence on septin organisation, we imaged septin incubated without an SLB. The septin coats the silicon wafer surface homogeneously with no visible alignment (figure 18C). We manually measured the width of the septin to be between 15 and 25 nm (black arrow figure 18C). We do not find bundled networks in the absence of an SLB, suggesting the SLB influences septins' bundling on a flat substrate.

We also found regions similar to the septin layer without an SLB (figure 18C) in the presence of an SLB (figure 18A), where in the same sample, we observed septin bundle networks (figure 18B). This observation implies the local absence of the SLB can be detected based on the structure of septin.

To further examine the influence of the membrane composition, we incubated hexamers on SLBs containing PI instead of PIP_2. Interestingly we found almost no septin binding to the bilayer, except for a few regions where we found bundles (figure 19). The bundles we observed, however, look significantly different from the bundles we observed on SLBs containing PIP_2. This observation would suggest septin to have a lower affinity to SLBs containing PI compared to PIP_2. This is contrary to our observation of TEM with lipid monolayers, where we find septin organises into meshwork for both PI and PIP_2 (figure 12).

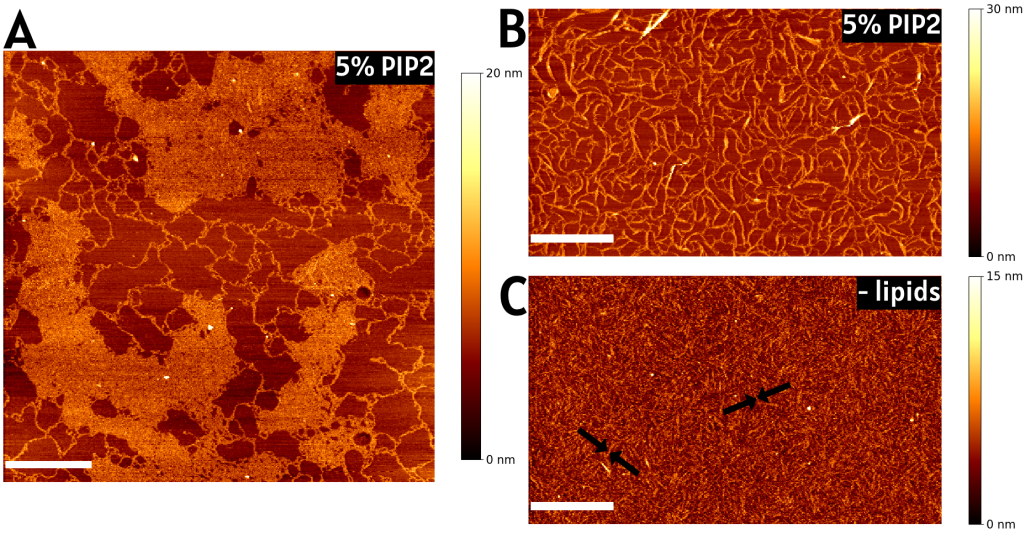

Figure 18: **The SLB influences septins' morphology.** (A, B) The AFM images show 120 nM septin hexamers incubated on a 5% PIP_2 SLB. The two images are two different regions from the same experiment. Septin organises into medium-density bundle networks (B) and coats the substrate (A). (C) The AFM image shows 120 nM hexamers incubated on bare silicon wafers. We find septin coats the substrate. The black arrows on the AFM image indicate the positions of hexamers. Scale bar: 2 µm.Colour bars on the right of the images display the height scale.

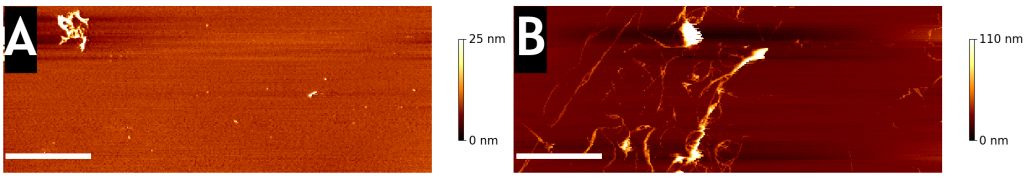

Figure 19: **Septin forms different organisations on 6% PI SLB compared to 5% PIP_2.** The AFM images show 120 nM septin hexamers on a 6% PI SLB fixed with 1% GTA. We find almost no septin binding, with the exception of a few bundles. Scale bar: 2 µm. Colour bars on the right of the images display the height scale.

4.2 Septin influence on membrane-bound actin networks

Recent research shows that septin plays an active role in membrane deformation [8, 24]. However, septin is also able to recruit actin at the membrane [6]. Actin recruitment has been speculated as one of the septin functions in the cortex. We reconstituted a septin-actin network on lipid layers to understand how septin might organise actin at the membrane. We also reconstituted Arp2/3-actin networks for comparison. Since Arp2/3 will nucleate actin at the membrane instead of recruiting filamentous actin, we expected to observe a difference in the actin morphology [72, 73]. We used TEM to examine the morphologies of the actin networks formed by these two actin-binding proteins.

4.2.1 Cortex reconstitution on glass-supported lipid bilayers

We first imaged our two reconstituted actin networks systems with TIRF microscopy. For this, we used glass-supported lipid bilayers formed by SUV fusion described in section 3.2 and section 3.3.1.

For the septin-actin network, we first incubated 50 nM septin octamers on 20% DOPS SLB (20:79.7:0.3 DOPS : DOPC : cy5-PE). After washing the sample with F-buffer, we added 1 µM of pre-polymerised actin. Figure 20 top row shows a representative fluorescence image, where we see a layer of septin on the SLB and septin colocalising with actin filaments. We also formed a septin-actin network on a DOPC SLB. Because Fly septin does not bind to DOPC lipids but does bind and bundle actin filaments [25], we also expect human septin only to interact with actin and form curved actin bundles [43]. As expected, we found no septin and actin filaments at the surface of the membrane (figure 20 bottom row). To still visualise the filaments, we added a crowding agent (0.15% methylcellulose) to push the protein to the lipid surface. In figure 20 middle row, we see the septin only colocalising with actin and no septin layer on the membrane. This result, in combination with the DOPC control, shows septin can recruit actin on an SLB in the presence of negatively charged lipids. And while we still see septin-actin bundles, the presence of a septin layer indicates the high affinity to the membrane.

The Arp2/3-actin networks are formed on bilayers composed of 2.5% NTA-DGS(Ni) SLB (2.5:97.2:0.3 DGS-NTA(ni) : DOPC : cy5-PE). We first let 200 nM of 10×His-tagged VCA domain bind to the Nickel-chelating lipids via its his-tag. After washing the unbound VCA, we add 50 nM Arp2/3 with 1 µM G-actin in imaging-buffer. We found actin filaments binding to the SLB, as shown in figure 21. To see if these networks are actin nucleated by Arp2/3 at the surface, we performed a control without VCA 21. Because the absence of VCA inhibits the nucleation by Arp2/3, we did not observe actin at the surface. Suggesting the actin is recruited at the membrane by VCA. We noticed that in the presence of the Arp2/3 and VCA, we found patches of higher actin filament density at the SLB. This patchy structure has been previously shown on SLBs [74] and could be caused by the autocatalytic nucleation of actin by Arp2/3.

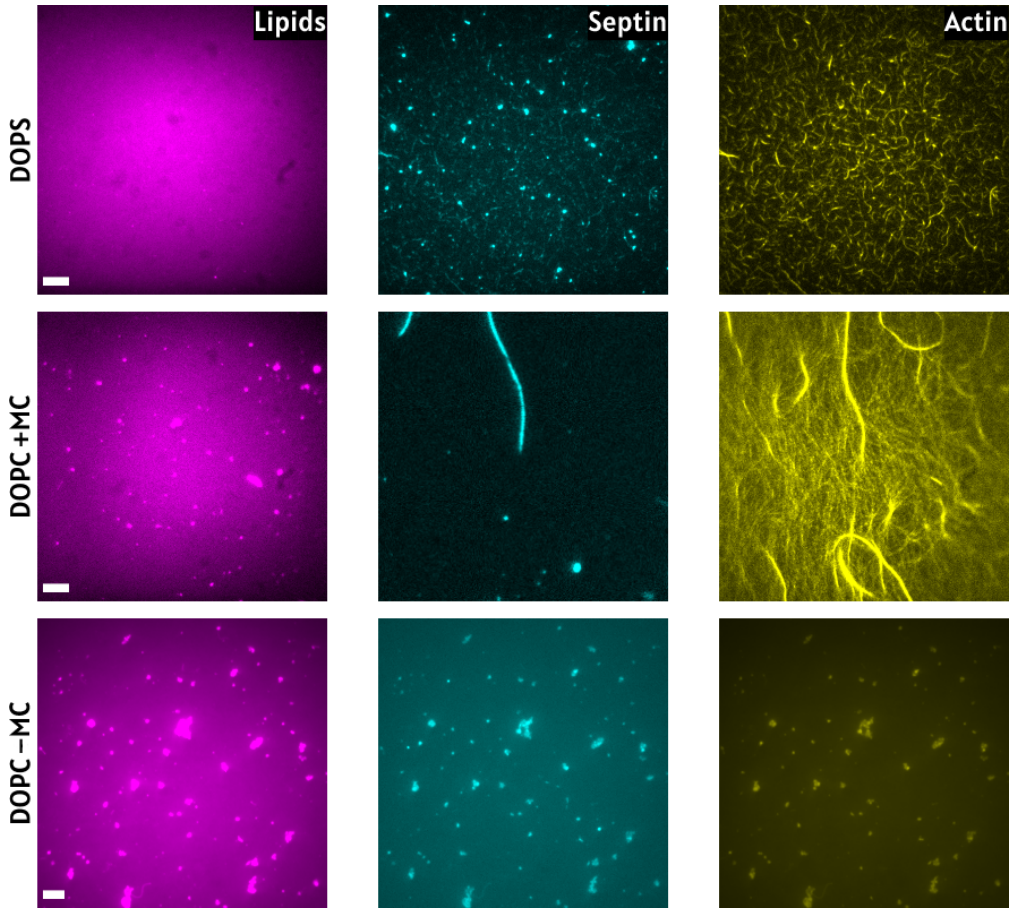

Figure 20: **Septin recruits actin at the 20% DOPS SLB.** TIRF acquisition of septin and actin incubated on a SLB in a flow channel. (top) Images (acquired from TIRF-1) show 500 nM octamers with 1 µM actin on a 20% DOPS SLB. (middle) Images (acquired from TIRF-1) show 300nM octamers with 1 µM actin and 0.15% MC on a 100% DOPC SLB.(bottom) Images (acquired from TIRF-2) show 300 nM octamers with 1 µM actin on a 100% DOPC SLB. Scale bar: 5 µm.

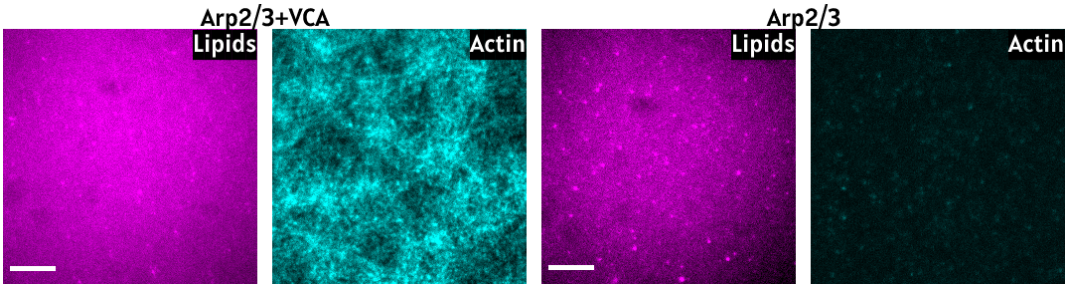

Figure 21: **The Arp2/3 complex in the presence of VCA nucleates actin on a 2.5% NTA-DGS(Ni) SLB.** TIRF images (acquired from TIRF-1) of 50 nM Arp2/3 and 1 µM actin incubated on a 2.5% NTA-DGS(Ni) SLB with and without 200nM VCA. Scale bar: 5 µm.

4.2.2 Electron microscopy imaging of septin-actin on lipid monolayers

Fluorescence microscopy reveals that septin could bundle actin or anchor actin to the membrane. We, therefore, used TEM to further examine the morphology of this interaction. To visualise the septin-actin network, we extended the protocols for septin incubated on a 5% PIP_2 monolayer, described in section 3.4. First, we formed a lipid monolayer in a well with 50 nM septin. Then, after transferring the monolayer to an EM-grid, we incubated the septin-decorated lipid monolayer with a solution of pre-polymerised actin for an hour. Finally, the sample was fixed and stained with 2% uranyl acetate and dried.

When we incubated pre-formed 50 nM hexamer or octamer meshworks on a 5% PIP_2 monolayer with 2 µM pre-formed actin filaments we observed long filaments (figure 22). The width of these longer filaments is around 7 nm correlating with the width of actin filaments [31]. And since septin did not form isolated long single filaments on 5% PIP_2 monolayers (figure 9), we identify these filaments as actin filaments. We also did not observe septin meshworks in figure 9. However, we might have insufficient contrast since the staining of this meshwork was inconsistent. Furthermore, we did not see many differences in actin networks between hexamers (figure 9A, B) and octamers (figure 9D, E), but this is only a tentative statement because we only had two experiments were the octamer-actin networks formed single filaments.

To see the lipid monolayer influence on the septin-actin networks, we co-incubated septin hexamers with actin filaments on a glow discharged carbon grid. We found septin and actin interacts, forming bundles (figure 22C, F). However, we also noticed fewer single actin filaments than in the case of pre-formed septin on a 5% PIP_2 monolayer incubated with pre-polymerised actin filaments. And while we did observe bundles for septin-actin on a lipid monolayer (figure 23), they were much less numerous than on a glow discharged grid.

We, unfortunately, did not perform a control experiment to see if we find actin binding to 5% PIP_2 monolayers. However, we would expect no actin-binding since TIRF microscopy revealed actin did not bind on 5% PIP_2 SLB (data not shown).

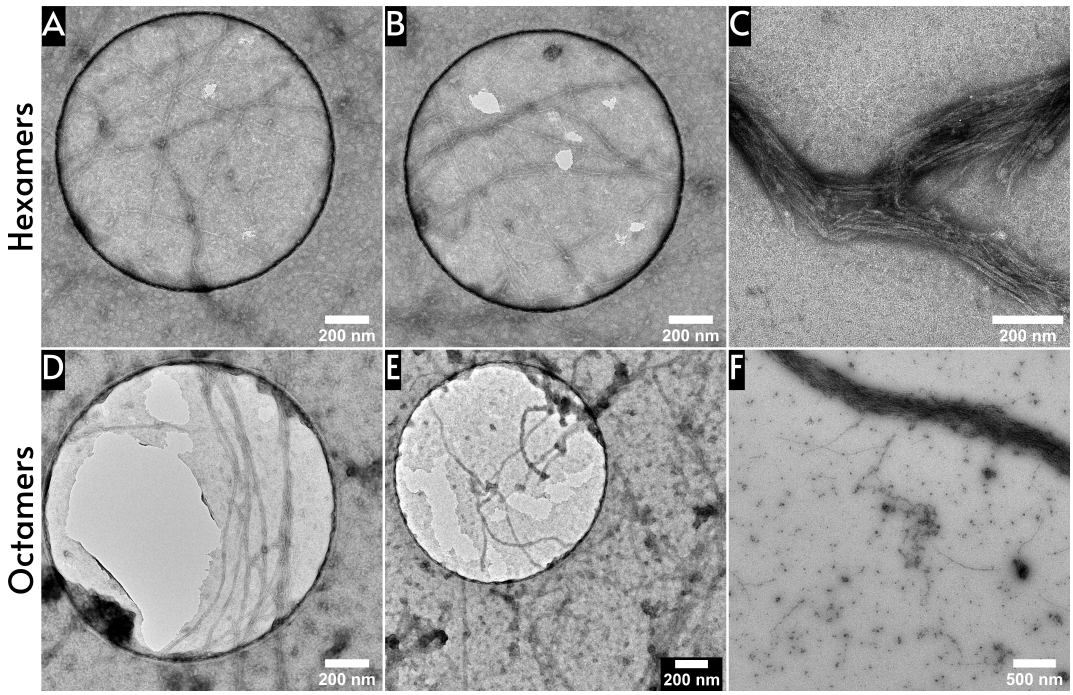

Figure 22: **Actin at 2 µM forms sparse single filament networks when co-incubated with septin on a 5% PIP_2 monolayers.** (A,B) TEM images of pre-formed 50 nM septin hexamers on a 5% PIP_2 monolayers co-incubated with 2 µM pre-polymerised actin. (D,E) TEM images of 50 nM septin octamers on a 5% PIP_2 monolayers co-incubated with 2 µM pre-polymerised actin. (C) TEM image of copolymerised 500 nM septin hexmers with 1 µM actin on a glow discharged carbon grid, acquired by MSc. Gerard Castro-Linares. (F) TEM image of copolymerised 500 nM septin octamers with 1 µM actin on a glow discharged carbon grid.

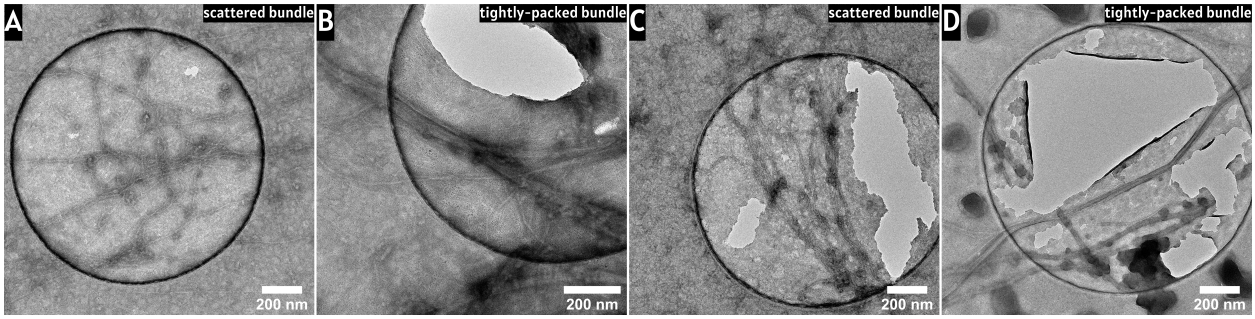

Figure 23: **Actin forms scattered bundles and tightly-packed bundles in the presence of septin hexamers on a lipid monolayers containing 5% PIP_2.** (A, B) TEM images of pre-formed 50 nM septin hexamers on a 5% PIP_2 monolayer incubated with 2 µM pre-polymersied actin. We found both the scattered bundles and (A) and tighly-packed budnles (B). (C, D) TEM images of 50 nM septin hexamers copolymerised with 2 µM actin on a 5% PIP_2 monolayer. We found both the scattered bundles and (C) and tighly-packed budnles (D).

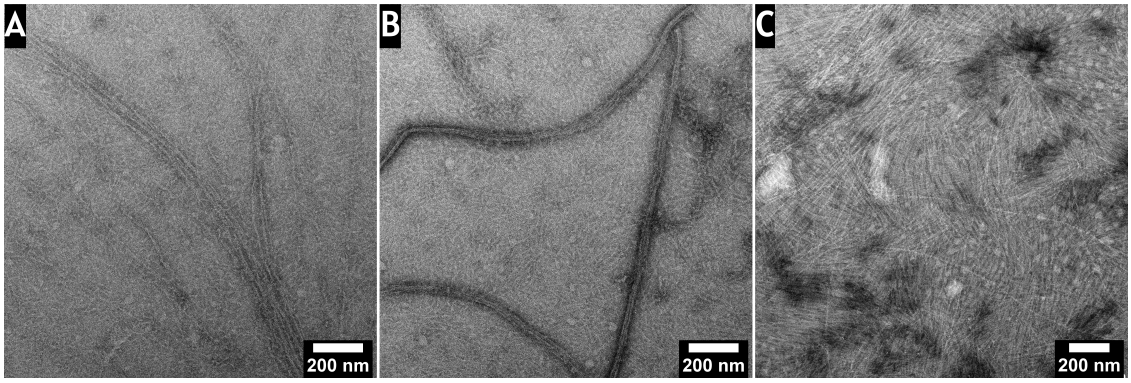

Figure 24: **Actin forms scattered bundles and tightly-packed bundles in the presence of septin octamers on a lipid monolayer containing 5% PIP_2.** TEM images of pre-formed 50 nM octamers on a 5% PIP_2 monolayer incubated with 1 µM pre-polymerised actin. We found both scattered bundles (A) and tightly-packed bundles (B). We also observed single actin filaments on top of a septin meshwork (C).

The actin filaments incubated with pre-formed septin hexamer on a 5% PIP_2 monolayer also seemed to form bundles (figure 23). We could differentiate two types of bundles, tightly packed aligned bundles (figure 23B) and more scattered bundles (figure 23A). We investigated if the bundle configuration is caused by the sequential incubation of pre-polymerised actin after septin was incubated on the monolayer. For this, we looked at bundles formed when septin and actin are copolymerised on the monolayer. We observed the same two types of bundles when copolymerising septin and actin on a lipid monolayer containing 5% PIP_2 (figure 23C and 23D). We also did not notice any frequency change in the number of bundles.

For the actin networks formed by incubating septin octamers on a 5% PIP_2 monolayers with 1 µM pre-polymerised actin, we have had a few experiments where we were able to observe a septin layer (similar to that observed in section4.1.2). These samples show similar two types of bundles as the septin hexamer-actin bundles (figure 24A and 24B). In addition, we can also see long single filaments resting on the septin network (figure 24C). We speculate these long filaments to be actin since we have not observed single septin filaments with a similar length when septin is incubated on a 5% PIP_2 monolayer (figure 9).

It would be interesting to explore the formation of the two types of bundles observed. The different bundle types might be explained by septin either interacting with actin in solution or at the membrane.

To see if the lipid composition affects the septin-actin organisation, we included 6% PI lipids instead of 5% PIP_2 in the monolayer. Human septin can bind to PI lipids shown by the septin meshwork formed by septin in figure 12C and 24A, B. While there is little evidence that suggests actin binds to lipids [75, 76], we surprisingly found actin at the 6% PI monolayer, forming meshwork (figure 24G, H). We did, however, not wash the sample before staining, which would reduce uranyl acetate stained unbound actin [77, 78].

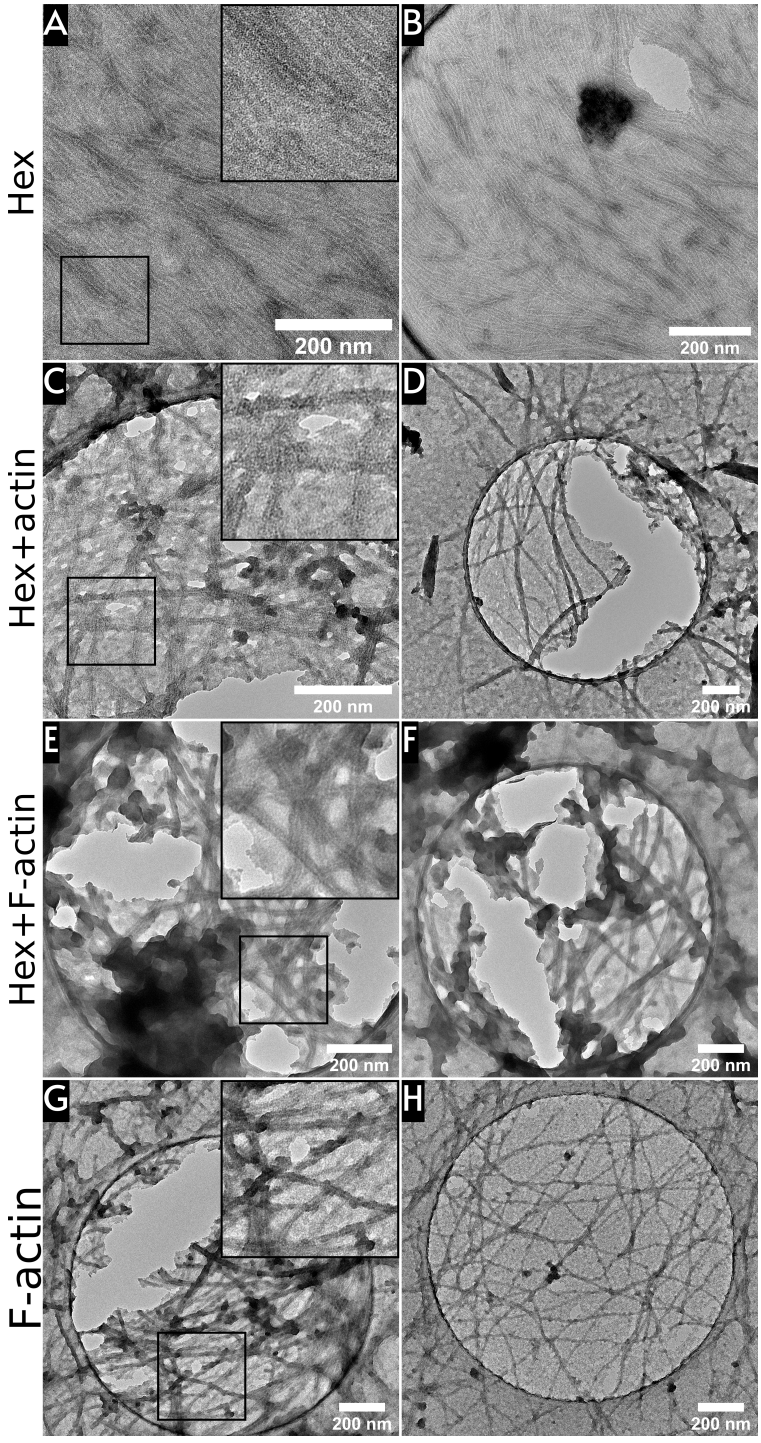

Figure 25: **TEM images show actin-septin meshworks on a 6% PI monolayer for 2µM actin.** (A, B) Two TEM images of 50 nM septin hexamer incubated on a 6% PI monolayer for the same sample. (C, D) Two TEM images of 50 nM septin hexamers copolymerised with 2 µM actin on a 6% PI monolayer for the same sample. (E, F) Two TEM images of pre-formed 50 nM septin hexamers on a 6% PI monolayer co-incubated with 2 µM pre-polymerised actin for the same sample. (G, H) Two TEM images of 2 µM actin incubated on a 6% PI monolayer for the same sample. Zoom ins on the septin-actin structure are shown in the insets of the figures.

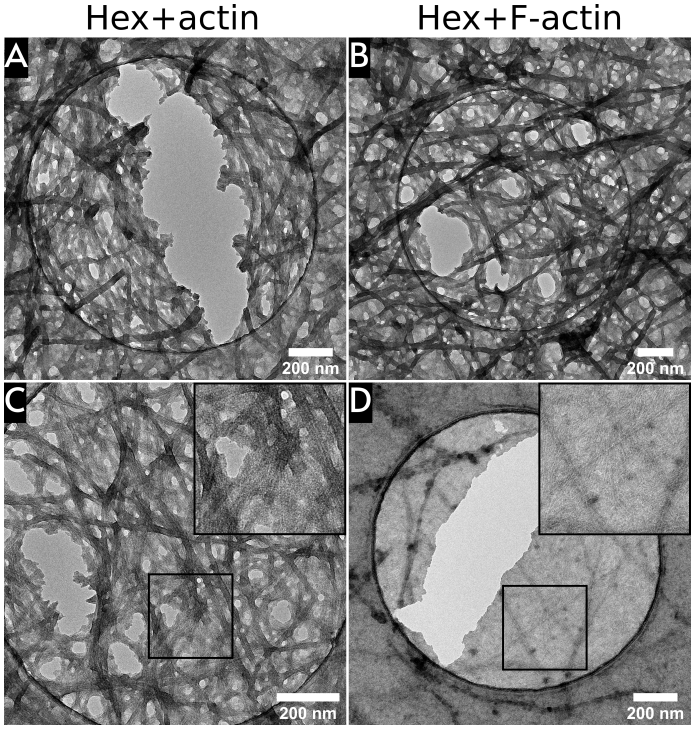

Figure 26: **TEM images show actin-septin meshworks on a 6% PI monolayer for 4µM actin.** (A, D) TEM images of 50 nM septin hexamer copolymerised with 4 µM actin on a 6% PI monolayer. (B, E) TEM images of pre-formed 50 nM septin hexamer on a 6% PI monolayer incubated with 4 µM pre-polymerised actin.

Dense filament networks were observed for the sequential incubation of 50 nM septin after 2 µM pre-polymerised actin (figure 25C, D). We also found dense filament meshworks when co-polymerising septin and actin on the lipid monolayer (figure 25E, F). We speculate the observed filaments to be actin since they looked similar to the actin filament we observed without septin (figures 25G, H). We find a higher actin filament density when incubating actin with pre-formed septin on 6% PI monolayer than on 5% PIP_2 monolayer. However, for the same experiment, we found different filament densities (figure 25E, F). Furthermore, we did not observe the septin-actin bundles on PI monolayers; however, the high filament density inside the meshworks made it difficult to detect bundles.

Next, we were interested in septin-actin network organisation on lipid monolayers for a higher actin concentration. We repeated the experiment for the septin-actin network on a 6% PI monolayer with an increased actin concentration of 4 µM. We observed an increase in filament density for 4 µM actin (figure 26A-C) compared to 2 µM (figure 25C-F). We did, however, also find a septin layer similar to the septin layer without actin (figure 25A, B) for the sequential incubation of septin hexamers after pre-polymerised actin on the monolayer (figure 26D). We did only observe this septin layer for 4 µ of actin (figure 26B, D) and not for 2 µM (figure 26B, D). These actin filaments on top of a membrane-bound septin meshwork (similar to observed in section 4.1.2) indicate that septin meshworks are able to recruit actin. Note that dense networks for 4 µM actin could also have septin meshworks obscured by the actin filaments. It would be interesting to see if these results can be replicated.

4.2.3 Electron microscopy imaging of Arp2/3-actin on lipid bilayers

We also imaged Arp2/3-actin networks with TEM to study the structural difference between septin-mediated recruitment of actin at the membrane compared to the nucleation of actin at the membrane by Arp2/3. To reconstitute these networks, we start by incubating 200 nM VCA on a 2.5% DGS-NTA(Ni) lipid monolayer. After 20 minutes, we incubated the VCA-coated monolayer with 2 or 4 µM G-actin and 50 nM Arp2/3.

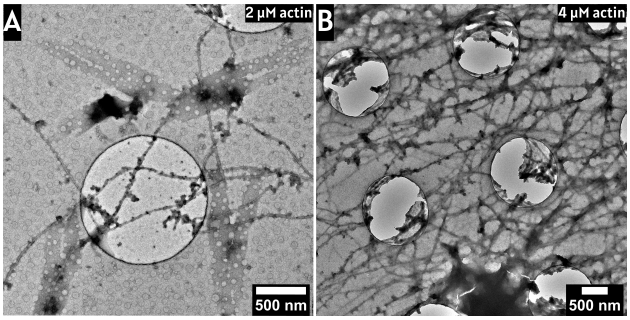

Figure 27: **Actin can form meshworks nucleated by Arp2/3.** TEM images of incubating 2 and 4 µM actin (A, B), respectively with 50nM Arp2/3 and 200nM VCA on a 2.5% DGS-NTA(Ni) containing lipid monolayer.

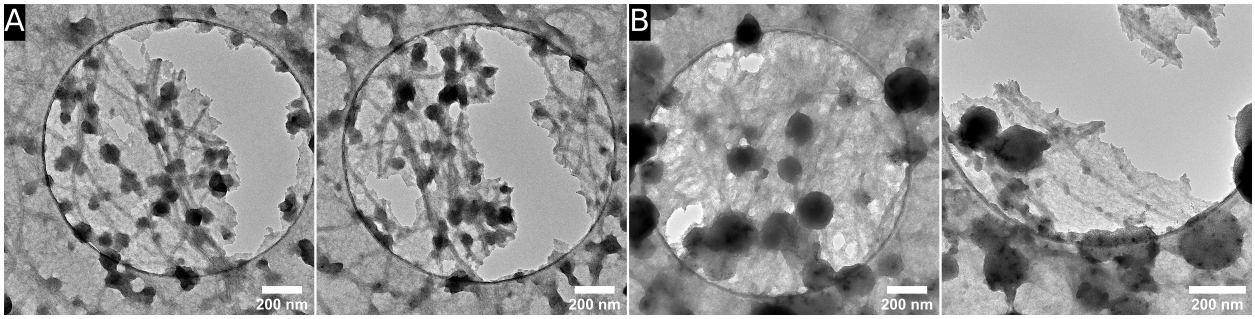

Figure 28: **Actin forms meshworks when incubated with Arp2/3 on 2.5% DGS-NTA(Ni) monolayers.** TEM images of 4µM actin incubated with 50nM Arp2/3 and 200nM VCA on a 2.5% DGS-NTA(Ni) monolayer. The figure shows two images for two different experiments (A, B).

In initial experiments with 2 µM actin, we mainly observed single actin filaments. We did, however, find local regions with multiple filaments (figure 27A). Since single actin filaments nucleated at the membrane did not look significantly different than single recruited actin filament by septin, we doubled the actin concentration to 4 µM. Similar to septin-actin networks, we observed actin meshworks with a heterogeneous filament density within the same sample (figure 27B).

To confirm actin nucleation by Arp2/3, we tried measuring the angle at nucleation sides since the Arp2/3 complex nucleates actin from preexisting actin filament at an angle of 70 °[40]. However, nucleation sites were difficult to find due to the dense meshwork. Instead, we manually measured 31 angles for six images at intersecting and touching filaments. We measured angles at 70°(figure 29), indicating we indeed found regions of Arp2/3 nucleated actin on a 2.5% DGS-NTA(Ni) monolayers. We also occasionally measured a 40°angle (figure 29). This 40°angle could be caused since we observed a projection of a three-dimensional actin network.

To confirm actin nucleation by Arp2/3, we repeated the experiments without VCA. We found fewer actin filaments in the absence of VCA (figure 30B), indicating actin and Arp2/3 did not bind to the monolayer. The remaining actin filaments could be present due to the lack of a washing step before staining.

We investigated the interaction with the carbon grid by incubating the actin with Arp2/3 and VCA without lipids. We found fewer actin filaments on the carbon grid without lipids (figure 30C) compared to with (figure 30A). We next investigated the influence of actin nucleating on a lipid monolayer instead of in solution by comparing the Arp2/3 nucleated networks on a lipid monolayer to Arp2/3 nucleated networks on glow discharged carbon. We found Arp2/3 nucleated network looked less dense on glow discharged grids compared to on lipid monolayers. The remaining filaments could be present due to the lack of a washing step. However, we did observe an increase in the number of filaments compared to non charged grids (figure 30 D). We, unfortunately, had insufficient data to draw a solid conclusion from this.

In 2 out of 5 experiments, we observed the Arp2/3-actin networks to show tightly packed bundles on lipid monolayers (figure 31A), similar to those observed in septin-actin networks (figure 23). These bundles were are also present in the absence of VCA (figure 31C). Furthermore, we observed actin bundles in the absence of a lipid monolayer (figure 31B), suggesting lipid interactions do not form the bundles. A previous study has also observed bundling of actin by Arp2/3 with TEM [79]. However, the bundling caused by Arp2/3 has not been mentioned after the discovery of its actin filament branching function[72]. We suspect bundling is caused by staining with uranyl acetate. It would be interesting to see if other stains also result in tightly packed actin bundles.

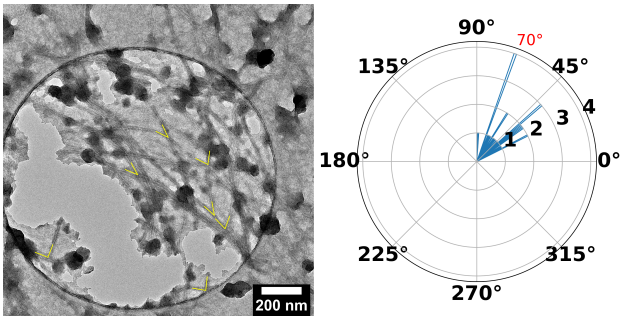

Figure 29: **Two main angles are observed between actin filaments for Arp2/3 nucleated actin on monolayers.** Example of a TEM image of 4µM actin incubated with 50nM Arp2/3 and 200nM VCA on a lipid monolayer on which we measured the angles between actin filaments. The yellow lines in the TEM image show locations where we measured the angle. The circular histogram shows the distribution of the 31 manually measured angles in six images.

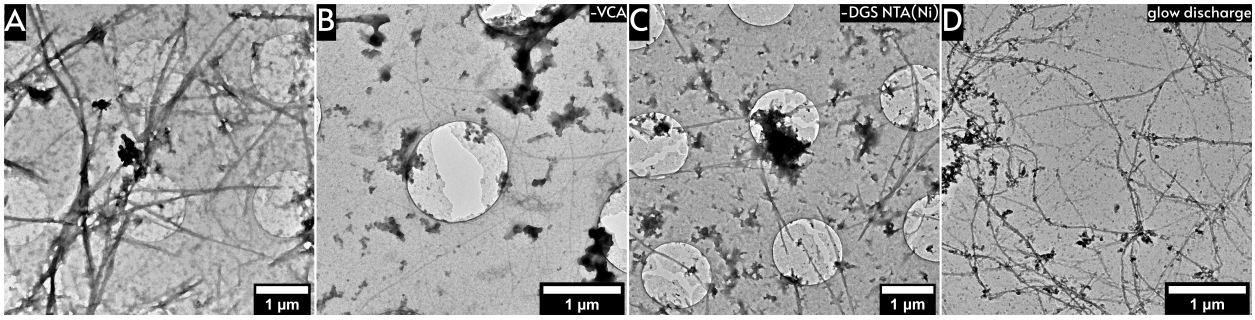

Figure 30: **TEM images of Arp2/3 nucleated actin cortex in presence and absence of lipid monolayer.** (A) TEM images of 4µM actin incubated with 50nM Arp2/3 and 200nM VCA on a 2.5% DGS-NTA(Ni) monolayer. (B) TEM images of 4µM actin incubated with 50nM Arp2/3 on a 2.5% DGS-NTA(Ni) monolayer. TEM images of 4µM actin incubated with 50nM Arp2/3 and 200nM VCA on a carbon grid. (D) TEM images of 4µM actin incubated with 50nM Arp2/3 and 200nM VCA on a glow discharged carbon grid.

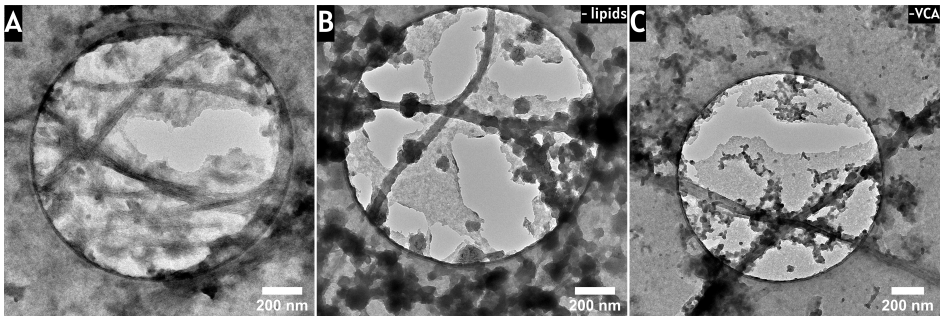

Figure 31: **TEM images shows tighly-packed bundled of actin in presence of Arp2/3 bundles.** (A) TEM images of 4µM actin incubated with 50nM Arp2/3 and 200nM VCA on a 2.5% DGS-NTA(Ni) monolayer. (B) TEM images of 4µM actin incubated with 50nM Arp2/3 and 200nM VCA on a carbon grid. (C) TEM images of 4µM actin incubated with 50nM Arp2/3 on a 2.5% DGS-NTA(Ni) monolayer.

5 Discussion

5.1 Membrane-bound septin network

In cells, septin localises on the plasma membrane, microtubules, and on actin stress fibres [6, 7, 27]. Septins' ability to deform and provide structure to the membrane and its role in actin recruitment make septin important for cell shape control. In this study, we imaged the organisation of human septin organisation on supported lipid membranes. While our membrane model simplifies the plasma membrane, we can still use these models to understand lipid septin interactions. We find that human septin interacts with PIP_2 lipids and forms filamentous layers that might provide the membrane with mechanical support.

5.1.1 Septin forms aligned networks on lipid monolayers

Using TEM, we observed cross-hatched structured meshworks of septin filaments when incubating septin on a 5% PIP_2 monolayers. We found this organisation for both human septin hexamers and human septin octamers. Analysis of the hexamer meshworks revealed arrays of paired filaments with spacing comparable to the length of a hexamer perpendicular to parallel aligned single filaments. We hypothesise hexamers inside the single filaments interact with the paired filaments, resulting in this regular spacing. It would be interesting to see if the analysis for the octamers meshworks will similarly reveal a regular spacing equal to the octamer length.

The structured networks of septin indicate that septin self-organises on the lipid monolayer by interactions with other septins. Septins' coiled-coil domains have been shown to hold paired filaments together [25, 65] and play an important role in septin-septin interaction. The hexamer interaction between the single and paired filaments could be mediated by the coiled-coil domains of different septin subunits, where one is still responsible for pairing filaments, another links the perpendicular arrays. Further experiments are needed to probe this theory. We suggest experiments imaging hexamers with specific mutations in their coiled-coils domains on PIP_2 monolayers to investigate if inhibition of paired filament arrays results in cross-hatched patterned meshworks of single septin filaments.

In order to form the observed networks, septin must also interact with the lipid monolayer. This raises the question if either the parallel aligned single filaments interact with the monolayer or the paired filaments arrays (or both). For yeast septin octamers, both single and paired filaments have been shown to interact with the membrane [8, 23]. Imaging of the cross-hatched networks on lipid monolayers with AFM [80] can confirm whether the single filaments interact with the membrane.

5.1.2 Septin forms a bundled network on bilayers

Using AFM, we observed bundled networks for hexamers incubating on 5% PIP_2 SLBs. For identical conditions, we find septin forms networks with different structural features, namely sparse, medium-density and dense bundle networks. In the dense and sparse networks, the bundles were curved. However, we only had a small number of repetitions for these experiments, and more repetitions are needed to investigate the difference between the different morphologies.

Interestingly, for the dense networks, which looked more similar to the fly septin networks reported in previous research [25], we found curved bundles with an average height above the surface of 9.6 nm. We noted this indicates the bundles vertically consist of two hexamers. However, for TEM, we measured the width of paired hexamer filament of 10 nm, suggesting the dense bundled networks might consist out of paired filaments. This could explain the difference with the medium dense networks, where we measured an average height above the surface of 5.7 nm, suggesting septin did not form paired filaments. We hypothesise that human septin needs to form paired filaments in order to form dense bundled networks on SLBs. Future experiments could investigate if these bundle networks form when paired filaments formation is suppressed

by a mutation in the coiled-coil domains [81].

We also investigate the dependency of septin concentration on bundle arrangement. While we showed thicker bundles for 120 nM than 60 nM, more data and analyses are necessary to draw conclusions. We speculate bundles could have a different function inside the cortex compared to filaments. It would be interesting to see for which concentration septin forms bundles and if bundle formation can be promoted by different lipid compositions.

5.1.3 Comparison between AFM and TEM findings

We find different organisations for septin incubated on SLB imaged with AFM than on lipid monolayers imaged with TEM. For the SLBs, we find curved bundle networks, while for the lipid monolayers, we find meshworks of paired filament and single filaments. We used a concentration of 120 nM septin hexamers in a volume of 100 µL for imaging septin on an SLB with AFM while using 50 nM septin hexamers in a volume of 30 or 100 µL for imaging septin on a lipid monolayer with TEM. The different total amount of septin per unit of area for AFM and TEM can be the cause of the different morphologies observed for the two methods [82]. We could increase the septin concentration for lipid monolayers, and we might find more bundles since bundles formation is increased for a higher concentration of septin [25]. We could also reduce the septin concentration for SLBs, and maybe find septin filament meshworks. However, for 60 nM of septin, we could not find any indication of cross-hatched meshworks. We are imaging by scanning the surface with a pyramidal tip which is 2 nm in radius, so this could hinder the imaging of a possible bottom layer. Further differences between the images could be explained by the different length scales of image size. We might not have a high lateral resolution to image filament meshworks with AFM. Comparing the AFM images to the TEM images with a similar time, we could only detect bundles and could not observe the meshworks (figure 32). However, this observation does not explain why we rarely found bundles with TEM imaging of septin on lipid monolayers.

Finally, the difference between our AFM and TEM data could be explained by the different nature of the lipid layers. Different lipid packing densities and fluidity between the supported lipid monolayer and bilayer could impact the organisation of septin on a model membrane.

Furthermore, we showed that human septin hexamers and octamers could bind to monolayers comprising of 6% PI. We, however, did not find septin when incubating hexamers on PI-containing SLBs. Since the SLB fluidity depends on the substrate, it could be that hexamers can bind to PI-containing SLBs. A fluorescence microscopy study of SLBs formed on a different substrate could be used to test if hexamers bind to PI SLBs.

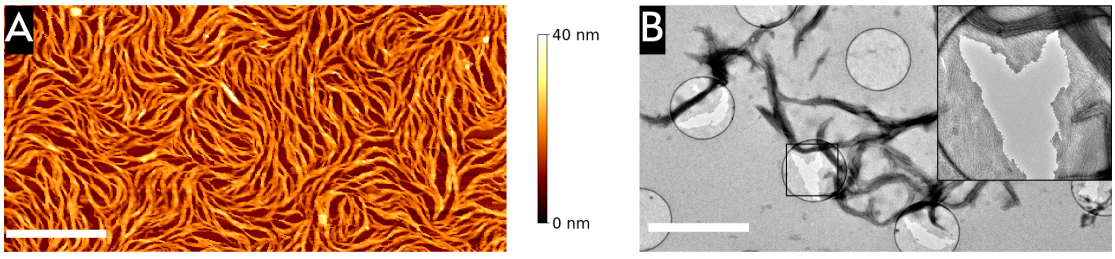

Figure 32: **Comparision between AFM and TEM images with the same scale** (A) AFM image of 100 nM human septin hexamers on 5% PIP_2 SLB, showing septin organising into dense bundle networks. (B) TEM image of 50 nM human septin hexamers on 5% PIP_2 SLB for the same size scale as AFM. At this scale, only the rarely found bundles could be identified. A zoom in on the septin structure is shown in the insets of the figure, which shows the septin filaments forming meshworks. Scale bars: 2 µm. The Colour bars on the right of the AFM image display the height scale.

5.2 Actin cortex reconstition on lipid monolayers

Using TEM, we imaged filamentous actin recruited by septin or nucleated by Arp2/3 on lipid monolayers. We observed dense networks of actin filaments on the lipid monolayers in both conditions. Actin was recruited at a random orientation by septin, while we could find the typical 70° angles for the Arp2/3 nucleated networks. Furthermore, we found bundles on lipid monolayers when incubating preformed actin filaments with membrane-bound septin.

While these observations show a decent proof of concept, the methodology needs to be improved before conclusions can be drawn. The first point of improvement is the washing of the sample. In order to get images with the highest contrast possible, we formed the lipid monolayers on carbon grids with holes. Imaging the monolayers suspended over these holes improved the image quality. To maintain the monolayer as intact as possible, we did not do washing steps between the incubations or before the staining. As a consequence, when we imaged actin, which only interacts by itself with positively charged lipids [76], in the absence of a membrane anchoring protein, we could still observe a dense network of filaments on the lipid monolayer. Washing steps between protein incubation steps could improve the unspecific binding of actin to the monolayer, giving a better representation of the actual anchored network. Further experiments could maybe use reinforcement of the lipid monolayer [80] to allow a washing step to remove unbound protein.

The second point of improvement would be to detect the presence of a lipid monolayer. We were able to observe covered holes in the carbon films when no monolayer was present (section 8.3). We tested the covering of the holes by incubation of F-buffer or MilliQ water and then fixating with uranyl acetate. We observed covered holes only when the samples were incubated with F-buffer and not with MilliQ. This shows the presence of covered holes does not indicate the presence of a monolayer. Optimisation of the lipid monolayer formation on EM-grids can be done by imaging fluorescently labelled monolayers with confocal microscopy [52]. Additionally, the lack of a monolayer on a covered carbon grid hole (or on a piece of the grid without holes) could explain why we sometimes obtained regions with single hexamers or octamers when incubating septin on a monolayer.

6 Conclusion

In this study, we successfully imaged the structures that humans septins formed on supported lipid membranes. TEM imaging of human septin on monolayers showed the formation of meshworks composed of paired filament arrays perpendicular to parallel single filaments. AFM imaging of human septin on SLB showed bundled networks of two filaments in height. These observations indicate that human septin forms organised structures by septin-septin and septin-membrane interaction on model membranes. If septin forms these organised structures on flat modelled membranes, it might also be the case that septin forms these structures on the plasma membrane. In cells, these septin meshworks could maybe provide the cell membrane with enhanced rigidity, act as a layer that could recruit proteins to the membrane, or act as a diffusive barrier. In addition, we showed a proof of concept for actin cortex reconstitution on monolayers, which allowed us to see actin recruitment by septin meshworks and compare it with actin networks formed by Arp2/3. This technique allows for high-resolution imaging of minimal cortices, allowing the study of the interaction between cortical proteins at a membrane interface. However, this technique needs further improvement to allow for a washing step. The formation of the cortex is also a crucial target for the reconstitution of synthetic cells. A synthetic cortex would allow the cell to control its shapes and provide mechanical stability. Reconstitution of minimal cortices on lipid monolayer allows for structural studies of the target proteins before reconstitution in a synthetic cell.

7 Acknowledgements

I would like to thank Prof. dr. Gijsje Koenderink, for this unique opportunity to do my master end project here, which used three different microscopy methods. This research group's openness to students is remarkable, in my opinion. Everyone in the group was eager to help each other and were genuinely interested in each other project. I especially want to thank Jeffrey den Haan for providing all proteins and helping in the lab when necessary. I also would like to thank Dr. Arjen Jakobi and Dr. Timon Idema for being on my assessment committee. Gerard and Lucia, I can not express my gratitude enough. Not only did I have the luxury of having two daily supervisors I also learned so much from each of them. Your guy's excitement for the cytoskeleton was contagious, and this project was not possible without your help. I wish both of you all the best in finishing your PhD.

References

[1] Ewa Paluch and Carl-Philipp Heisenberg. "Biology and physics of cell shape changes in development". In: *Current Biology* 19.17 (2009), R790–R799.

[2] Thomas Lecuit and Pierre-Francois Lenne. "Cell surface mechanics and the control of cell shape, tissue patterns and morphogenesis". In: *Nature reviews Molecular cell biology* 8.8 (2007), pp. 633–644.

[3] Kevin J Chalut and Ewa K Paluch. "The actin cortex: a bridge between cell shape and function". In: *Developmental cell* 38.6 (2016), pp. 571–573.

[4] Gijsje H Koenderink and Ewa K Paluch. "Architecture shapes contractility in actomyosin networks". In: *Current opinion in cell biology* 50 (2018), pp. 79–85.

[5] Maté Biro et al. "Cell cortex composition and homeostasis resolved by integrating proteomics and quantitative imaging". In: *Cytoskeleton* 70.11 (2013), pp. 741–754.

[6] Serge Mostowy and Pascale Cossart. "Septins: the fourth component of the cytoskeleton". In: *Nature reviews Molecular cell biology* 13.3 (2012), pp. 183–194.

[7] Andrew A Bridges and Amy S Gladfelter. "Septin form and function at the cell cortex". In: *Journal of Biological Chemistry* 290.28 (2015), pp. 17173–17180.

[8] Alexandre Beber et al. "Membrane reshaping by micrometric curvature sensitive septin filaments". In: *Nature communications* 10.1 (2019), pp. 1–12.

[9] Agata Szuba. "Deconstruction of septin assembly". PhD thesis. Amsterdam,Netherlands: Vrije Universiteit Amsterdam, 2019.

[10] JH Lorent et al. "Plasma membranes are asymmetric in lipid unsaturation, packing and protein shape". In: *Nature chemical biology* 16.6 (2020), pp. 644–652.

[11] Bruce Alberts et al. "The lipid bilayer". In: *Molecular Biology of the Cell. 4th edition*. Garland Science, 2002.

[12] Geoffrey M Cooper. "Structure of the plasma membrane". In: *The cell: A molecular approach* 2 (2000).

[13] Zachary T Graber et al. "Phosphatidylinositol-4, 5-bisphosphate ionization and domain formation in the presence of lipids with hydrogen bond donor capabilities". In: *Chemistry and physics of lipids* 165.6 (2012), pp. 696–704.

[14] Chris Janetopoulos and Peter Devreotes. "Phosphoinositide signaling plays a key role in cytokinesis". In: *The Journal of cell biology* 174.4 (2006), pp. 485–490.

[15] Keith Burridge et al. "Actin—membrane interaction in focal adhesions". In: *Cell Differentiation and Development* 32.3 (1990), pp. 337–342.

[16] Minhajuddin Sirajuddin et al. "Structural insight into filament formation by mammalian septins". In: *Nature* 449.7160 (2007), pp. 311–315.

[17] Sangdun Choi. *Encyclopedia of Signaling Molecules*. Vol. 337. Springer New York, 2012.

[18] Jeroen Dobbelaere and Yves Barral. "Spatial coordination of cytokinetic events by compartmentalization of the cell cortex". In: *Science* 305.5682 (2004), pp. 393–396.

[19] Fabrice Caudron and Yves Barral. "Septins and the lateral compartmentalization of eukaryotic membranes". In: *Developmental cell* 16.4 (2009), pp. 493–506.

[20] Michael A McMurray and Jeremy Thorner. "Turning it inside out: the organization of human septin heterooligomers". In: *Cytoskeleton* 76.9-10 (2019), pp. 449–456.

[21] Deborah C Mendonça et al. "A revised order of subunits in mammalian septin complexes". In: *Cytoskeleton* 76.9-10 (2019), pp. 457–466.

[22] Forooz Soroor et al. "Revised subunit order of mammalian septin complexes explains their in vitro polymerization properties". In: *Molecular biology of the cell* 32.3 (2021), pp. 289–300.

[23] Aurélie Bertin et al. "Phosphatidylinositol-4, 5-bisphosphate promotes budding yeast septin filament assembly and organization". In: *Journal of molecular biology* 404.4 (2010), pp. 711–731.

[24] Yohko Tanaka-Takiguchi, Makato Kinoshita, and Kingo Takiguchi. "Septin-mediated uniform bracing of phospholipid membranes". In: *Current Biology* 19.2 (2009), pp. 140–145.

[25] Agata Szuba et al. “Membrane binding controls ordered self-assembly of animal septins”. In: *Elife* 10 (2021), e63349.

[26] Kevin S Cannon et al. “An amphipathic helix enables septins to sense micrometer-scale membrane curvature”. In: *Journal of Cell Biology* 218.4 (2019), pp. 1128–1137.

[27] Elias T Spiliotis. “Spatial effects- site-specific regulation of actin and microtubule organization by septin GTPases”. In: *Journal of cell science* 131.1 (2018), jcs207555.

[28] Yi-Wen Heng and Cheng-Gee Koh. “Actin cytoskeleton dynamics and the cell division cycle”. In: *The international journal of biochemistry & cell biology* 42.10 (2010), pp. 1622–1633.

[29] Matthias Schaks, Grégory Giannone, and Klemens Rottner. “Actin dynamics in cell migration”. In: *Essays in biochemistry* 63.5 (2019), pp. 483–495.

[30] Roberto Dominguez and Kenneth C Holmes. “Actin structure and function”. In: *Annual review of biophysics* 40 (2011), pp. 169–186.

[31] Geoffrey M Cooper. “Structure and organization of actin filaments”. In: *The cell: a molecular approach* 2 (2000).

[32] Elif Nur Firat-Karalar and Matthew D Welch. “New mechanisms and functions of actin nucleation”. In: *Current opinion in cell biology* 23.1 (2011), pp. 4–13.

[33] Ricardo Uribe and David Jay. “A review of actin binding proteins: new perspectives”. In: *Molecular biology reports* 36.1 (2009), pp. 121–125.

[34] Priyamvada Chugh and Ewa K Paluch. “The actin cortex at a glance”. In: *Journal of cell science* 131.14 (2018).

[35] Tatyana M Svitkina. “Actin cell cortex: structure and molecular organization”. In: *Trends in cell biology* (2020).

[36] Julia Gilden and Matthew F Krummel. “Control of cortical rigidity by the cytoskeleton: emerging roles for septins”. In: *Cytoskeleton* 67.8 (2010), pp. 477–486.

[37] Laurent Blanchoin et al. “Actin dynamics, architecture, and mechanics in cell motility”. In: *Physiological reviews* 94.1 (2014), pp. 235–263.

[38] Cornelia Schwayer et al. “Actin rings of power”. In: *Developmental Cell* 37.6 (2016), pp. 493–506.

[39] Vassilis Papalazarou and Laura M Machesky. “The cell pushes back: The Arp2/3 complex is a key orchestrator of cellular responses to environmental forces”. In: *Current opinion in cell biology* 68 (2021), pp. 37–44.

[40] Kurt J Amann and Thomas D Pollard. “The Arp2/3 complex nucleates actin filament branches from the sides of pre-existing filaments”. In: *Nature cell biology* 3.3 (2001), pp. 306–310.

[41] Shae B Padrick et al. “Arp2/3 complex is bound and activated by two WASP proteins”. In: *Proceedings of the National Academy of Sciences* 108.33 (2011), E472–E479.

[42] Katja Schmidt and Benjamin J Nichols. “Functional interdependence between septin and actin cytoskeleton”. In: *BMC cell biology* 5.1 (2004), pp. 1–13.

[43] Manos Mavrakis et al. “Septins promote F-actin ring formation by crosslinking actin filaments into curved bundles”. In: *Nature cell biology* 16.4 (2014), pp. 322–334.

[44] Jean-Yves Tinevez et al. “Role of cortical tension in bleb growth”. In: *Proceedings of the National Academy of Sciences* 106.44 (2009), pp. 18581–18586.

[45] Guillaume T Charras et al. “Reassembly of contractile actin cortex in cell blebs”. In: *The Journal of cell biology* 175.3 (2006), pp. 477–490.

[46] Miia Bovellan et al. “Cellular control of cortical actin nucleation”. In: *Current Biology* 24.14 (2014), pp. 1628–1635.

[47] Colleen T Skau and Clare M Waterman. “Specification of architecture and function of actin structures by actin nucleation factors”. In: *Annual review of biophysics* 44 (2015), pp. 285–310.

[48] Alfredo Erazo-Oliveras et al. “Functional link between plasma membrane spatiotemporal dynamics, cancer biology, and dietary membrane-altering agents”. In: *Cancer and Metastasis Reviews* 37.2 (2018), pp. 519–544.

[49] Joe Sarkis and Véronique Vié. "Biomimetic Models to Investigate Membrane Biophysics Affecting Lipid–Protein Interaction". In: *Frontiers in bioengineering and biotechnology* 8 (2020), p. 270.

[50] Sven K Vogel. "Reconstitution of a minimal actin cortex by coupling Actin Filaments to Reconstituted Membranes". In: *Cytoskeleton Methods and Protocols*. Springer, 2016, pp. 213–223.

[51] Luke A Clifton et al. "Design and use of model membranes to study biomolecular interactions using complementary surface-sensitive techniques". In: *Advances in colloid and interface science* 277 (2020), p. 102118.

[52] Sven K Vogel et al. "The design of MACs (minimal actin cortices)". In: *Cytoskeleton* 70.11 (2013), pp. 706–717.

[53] Fabian Heinemann, Sven K Vogel, and Petra Schwille. "Lateral membrane diffusion modulated by a minimal actin cortex". In: *Biophysical journal* 104.7 (2013), pp. 1465–1475.

[54] Deborah F Kelly, Danijela Dukovski, and Thomas Walz. "A practical guide to the use of monolayer purification and affinity grids". In: *Methods in enzymology* 481 (2010), pp. 83–107.

[55] Manos Mavrakis, F-C Tsai, and Gijsje H Koenderink. "Purification of recombinant human and drosophila septin hexamers for TIRF assays of actin–septin filament assembly". In: *Methods in cell biology* 136 (2016), pp. 199–220.

[56] Francois Iv et al. "Insights into animal septins using recombinant human septin octamers with distinct SEPT9 isoforms". In: *bioRxiv* (2021).

[57] Ganzinger KA Sonal et al. "Myosin-II activity generates a dynamic steady state with continuous actin turnover in a minimal actin cortex". In: *J. Cell Sci* 132 (2018).

[58] Gregory J Hardy, Rahul Nayak, and Stefan Zauscher. "Model cell membranes: Techniques to form complex biomimetic supported lipid bilayers via vesicle fusion". In: *Current opinion in colloid & interface science* 18.5 (2013), pp. 448–458.

[59] Ralf P Richter, Rémi Bérat, and Alain R Brisson. "Formation of solid-supported lipid bilayers: an integrated view". In: *Langmuir* 22.8 (2006), pp. 3497–3505.

[60] Egidijus E Uzgiris and Roger D Kornberg. "Two-dimensional crystallization technique for imaging macromolecules, with application to antigen–antibody–complement complexes". In: *Nature* 301.5896 (1983), pp. 125–129.

[61] Stephen T. Ross et al. *Total internal reflection fluorescence (TIRF) microscopy*. URL: `https://www.microscopyu.com/techniques/fluorescence/total-internal-reflection-fluorescence-tirf-microscopy`.

[62] David Nečas and Petr Klapetek. "Gwyddion: an open-source software for SPM data analysis". In: *Open Physics* 10.1 (2012), pp. 181–188.

[63] Elias T Spiliotis and Michael A McMurray. "Masters of asymmetry–lessons and perspectives from 50 years of septins". In: *Molecular Biology of the Cell* 31.21 (2020), pp. 2289–2297.

[64] Benjamin L Woods and Amy S Gladfelter. "The state of the septin cytoskeleton from assembly to function". In: *Current opinion in cell biology* 68 (2021), pp. 105–112.

[65] Aurelie Bertin et al. "Saccharomyces cerevisiae septins: supramolecular organization of heterooligomers and the mechanism of filament assembly". In: *Proceedings of the National Academy of Sciences* 105.24 (2008), pp. 8274–8279.

[66] Antonio Casamayor and Michael Snyder. "Molecular dissection of a yeast septin: distinct domains are required for septin interaction, localization, and function". In: *Molecular and cellular biology* 23.8 (2003), pp. 2762–2777.

[67] Jianshe Zhang et al. "Phosphatidylinositol polyphosphate binding to the mammalian septin H5 is modulated by GTP". In: *Current Biology* 9.24 (1999), pp. 1458–1467.

[68] Yang Gan. "Atomic and subnanometer resolution in ambient conditions by atomic force microscopy". In: *Surface Science Reports* 64.3 (2009), pp. 99–121.

[69] Charlotte A Scarff et al. "Variations on negative stain electron microscopy methods: tools for tackling challenging systems". In: *Journal of visualized experiments: JoVE* 132 (2018).

[70] Muhammad Shuja Khan, Noura Sayed Dosoky, and John Dalton Williams. "Engineering lipid bilayer membranes for protein studies". In: *International journal of molecular sciences* 14.11 (2013), pp. 21561–21597.

[71] Zhengjian Lv et al. "Supported lipid bilayers for atomic force microscopy studies". In: *Nanoscale Imaging*. Springer, 2018, pp. 129–143.

[72] Fumihiko Nakamura et al. "Comparison of Filamin A-induced Cross-linking and Arp2/3 Complex-mediated Branching on the Mechanics of Actin Filaments* 210". In: *Journal of Biological Chemistry* 277.11 (2002), pp. 9148–9154.

[73] Casey A Ydenberg et al. "Cease-fire at the leading edge: new perspectives on actin filament branching, debranching, and cross-linking". In: *Cytoskeleton* 68.11 (2011), pp. 596–602.

[74] Shachar Gat et al. "Finger-like membrane protrusions are favored by heterogeneities in the actin network". In: *Soft Matter* 16.31 (2020), pp. 7222–7230.

[75] Dominique St-Onge and Claude Gicquaud. "Evidence of direct interaction between actin and membrane lipids". In: *Biochemistry and Cell Biology* 67.6 (1989), pp. 297–300.

[76] Carsten FE Schroer et al. "Charge-dependent interactions of monomeric and filamentous actin with lipid bilayers". In: *Proceedings of the National Academy of Sciences* 117.11 (2020), pp. 5861–5872.

[77] Ying-Wu Lin. "Uranyl binding to proteins and structural-functional impacts". In: *Biomolecules* 10.3 (2020), p. 457.

[78] O Pible et al. "Structural insights into protein–uranyl interaction: towards an in silico detection method". In: *Biochimie* 88.11 (2006), pp. 1631–1638.

[79] R Dyche Mullins et al. "Arp2/3 complex from Acanthamoeba binds profilin and cross-links actin filaments". In: *Molecular biology of the cell* 9.4 (1998), pp. 841–852.

[80] Anne Simon et al. "Free-standing lipid films stabilized by Annexin-A5". In: *Biochimica et Biophysica Acta (BBA)-Biomembranes* 1828.11 (2013), pp. 2739–2744.

[81] Elizabeth A Booth et al. "Effects of Bni5 binding on septin filament organization". In: *Journal of molecular biology* 428.24 (2016), pp. 4962–4980.

[82] Elisa Godino et al. "Cell-free biogenesis of bacterial division proto-rings that can constrict liposomes". In: *Communications biology* 3.1 (2020), pp. 1–11.

[83] Heiko M Seeger et al. "Supported lipid bilayers on mica and silicon oxide: comparison of the main phase transition behavior". In: *The Journal of Physical Chemistry B* 114.27 (2010), pp. 8926–8933.

[84] Magdalena Przybylo et al. "Lipid diffusion in giant unilamellar vesicles is more than 2 times faster than in supported phospholipid bilayers under identical conditions". In: *Langmuir* 22.22 (2006), pp. 9096–9099.

[85] Hanna P Wacklin. "Composition and asymmetry in supported membranes formed by vesicle fusion". In: *Langmuir* 27.12 (2011), pp. 7698–7707.

[86] Ryugo Tero. "Substrate effects on the formation process, structure and physicochemical properties of supported lipid bilayers". In: *Materials* 5.12 (2012), pp. 2658–2680.

[87] Nam-Joon Cho et al. "Comparison of extruded and sonicated vesicles for planar bilayer self-assembly". In: *Materials* 6.8 (2013), pp. 3294–3308.

[88] Artur Matysik and Rachel S Kraut. "Preparation of mica supported lipid bilayers for high resolution optical microscopy imaging". In: *JoVE (Journal of Visualized Experiments)* 88 (2014), e52054.

[89] DM Czajkowsky and Z Shao. "Inhibition of protein adsorption to muscovite mica by monovalent cations". In: *Journal of microscopy* 211.1 (2003), pp. 1–7.

8 Appendix

8.1 Mica-supported lipid bilayers

During this project, we tried mica as a substrate for our SLB supported reconstituted cortices. Mica is a transparent crystalline substrate with cleavable layers. Cleaving mica leaves a flat hydrophilic surface on which an SLB can be formed. We then reconstitute the septin cortex by adding septin.

Because the membrane fluidity depends on the substrate [83–86], we perform FRAP-recovery assays. During these assays, we also bind septin to see if the lipids can still bind septin.

8.1.1 Method

SUV formation
We used the same SUV formation previously described (section 3.1). However, we also attempted to replace the sonication step after freeze-thawing with an extrusion step. We extruded the SUVs at room temperature through 100 nm polycarbonate membranes (800309, Whatman) by an Avanti Mini-Extruder (Avanti Polar Lipids) following the manufacturer's directions. We used the extruded SUVs immediately after extrusion because they are vulnerable to ageing [87].

Device preparation

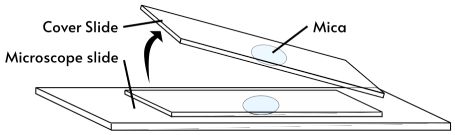

Figure 33: **Mica sandwich technique to form a thin layer of mica on cover slides.** Glass-mica-glass sandwich assembled by glueing mica between a cover slide and microscope slide. Disassembly of the glass-mica-glass sandwich results in a thin layer of cleaved mica on the cover slide.

The mica purchased from Agar Scientific (AGG250-1, Agar Scientific) is prepared for imaging using a modified approach to a previously established method for preparing for SLB formation [88]. First, from the mica sheet, a disk with a radius of 7/16 inches is stamped using a punch and die set (Precision Brand). Next, the disk is cut into thinner leaflets with a sharp blade, after which it is glued with optical adhesive (Norland Optical Adhesive 81) to a microscope slide (76 x 26 mm, thickness: 0.1mm, Menzel Gläser). Next, the adhesive is cured under a UV lamp (Walther Pro Flashlight UV5) with a wavelength of 395 nm for a minimum of 2 minutes. Then, when the adhesive is cured, the exposed mica is cleaved with scotch tape and glued with optical adhesive to a cover slide (24 x 60 mm, thickness: 0.15mm, Menzel Gläser) to form a sandwich of microscope-slide, mica, and coverslip.

The coverslip is split from the mica sandwich by gently lifting the coverslip using a razor blade. A thin layer of freshly cleaved mica remains on top of the coverslip.

SLB formation
On this surface 20 µL of F-buffer with 8 mM $MgCl_2$ is added. Immediately after, 20 µL of 0.2 mM SUVs in F-buffer are added. The salt concentration is increased to promote SUV rupture and, therefore, SLB formation. After 30 minutes, excess unbound lipids were washed off by replacing the liquid with x µL of F-buffer and leaving 10 µL.

We follow the washing by adding 10 µL of human septin octamers with the desired concentration in polymerisation-buffer with 1 mM MgGTP. After at least 20 minutes, the unbound septin is washed off by replacing the liquid with 60 µL of F-buffer, leaving 20 µL.

8.1.2 Results

Before using the mica-supported lipid bilayer with AFM, we imaged SLBs with TIRF microscopy to optimise the SLB formation. We co-polymerised 100 nM or 150 nM human septin octamers with 10% GFP-labeled septin in imaging-buffer with 1 mM MgGTP on a 20% DOPS SLB. We first investigated if sonicated or extruded SUVs would give more consistent SLB formation since extruded, and sonicated are both used for vesicle fusion [86]. We observed an intensity signal for the lipids that appeared more homogenous for the SLB formed by sonicated SUVs (figure 34A) compared to the dark-spotted signal from the SLB formed by extruded SUVs (figure 34D). We also observed a more homogenous intensity signal for the septin for the SLB formed by sonicated SUVs (figure 34A) compared to the bright spotted signal from the extruded SUVs (figure 34D). The bright spots of septin colocalises with the dark spots of the lipids. We do note that we did also have experiments where we found these spots for sonicated SUVs. Since mica can adsorb a number of different proteins [89], we speculate the extruded SUVs formed SLBs with holes where the septin will bind.

To verify the fluidity of the SLBs, we performed a FRAP assay (section 3.5.1). We observed similar results to glass supported lipid bilayers (section 4.1.1) for both extruded SUVs and sonicated SUVs, where the fluorescence signal in the FRAP regions recovers for the lipids and not for the septin (figure 34). While we did not analyse the FRAP measurements, we did measure inconsistent recovery times for both the extruded SUVs and sonicated SUVs (Figure 34C, F). Furthermore, the SLB formation on mica showed poor reproducibility, with several different artefacts observed for the lipid membranes. Examples of artefacts we observed were lipid tubes and lipids islands.

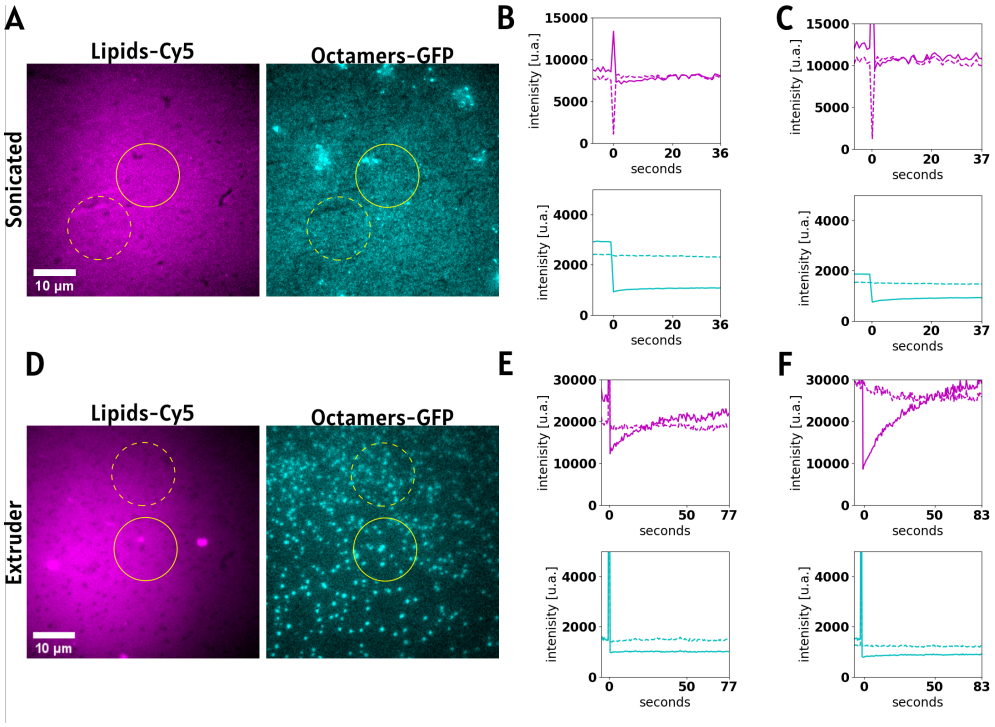

Figure 34: **Optimising SLB formation on Mica.** (A, B) TIRF images (acquired from TIRF-1) of octamers on 20 % DOPS mica-supported lipid bilayer. The solid circle indicates the FRAP region. (A) Images of 150 nM octamers on an SLB formed from sonicated SUVs. (B) Images of 100 nM octamers on an SLB formed from extruded SUVs. (B, E) The FRAP measurements of shown fluorescent images. (C, F) Different examples of FRAP of measurements on SLB formed from sonicated SUVs (C) and extruded SUVs (F).

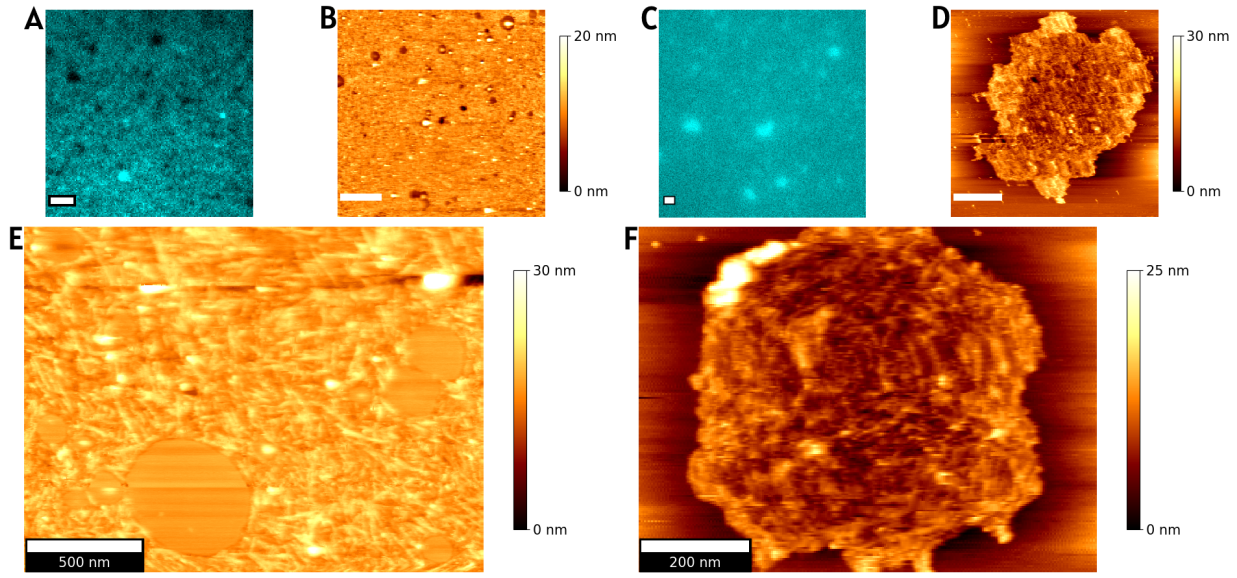

Figure 35: **AFM AC-mode height images of incubated septin on mica-supported lipid bilayer showed either a layer with holes or islands.** (A, B, E) Images of 50 nM octamers incubated on 20 % DOPS SLBs formed from sonicated SUVs. (A) TIRF image (acquired from TIRF-1) showing holes in the septin layer. (B, E) AFM images show a septin layer with holes. (C, D, F) Images of 100 nM octamers incubated on 20% DOPS formed from extruded SUVs. (C) TIRF image (acquired from TIRF-1) shows clusters of septin. (D, F) AFM images show septin islands. Scale bars of the top images is 1 µm. Colour bars on the right of the AFM images display the height scale.

Next, we imaged the co-polymerised human septin octamers with 10% GFP-labeled septin in polymerisation-buffer with 1 mM MgGTP on a 20% DOPS SLB with AFM. We found for different experiments that the septin either forms a layer with holes (figure 35A) or forms islands (figure 35). Zooming in on the layer with holes, we observe the holes to be flat. We also imaged the same experiments with TIRF microscopy and found holes in the septin layer for the layer with holes and dots for the islands. The absence of septin for the holes in the layer suggests these regions might be unwashed SUVs that burst after the first scan with AFM. For the island, these might have been holes in the SLB, which lead to septin binding to the mica.

Because of these initial results, we hypothesise septin shows affinity to mica. For this project, we did not follow up on this and imaged septin incubated on silicon wafer-supported bilayers.

8.2 Monolayer lipid composition

The lipid monolayer is formed by dropping lipids in chloroform on a well. The table below shows the volume and total lipid concentration of the lipid drop and the type of wells for each figure shown in section 4.1.2 and 4.2.

Figure	**Well**	**Volume drop**	**Concentration**
9A-E	30µL-well	2 µL	0.01 mM
9F	30µL-well	2 µL	0.005 mM
10	30µL-well	2 µL	0.005 mM
11A	30µL-well	2 µL	0.01 mM
11D	30µL-well	2 µL	0.005 mM
12A	100µL-well	2 µL	0.01 mM
12B	30µL-well	2 µL	0.01 mM
12C	100µL-well	0.5 µL	0.1 mM
12D	100µL-well	2 µL	0.005mM
22AB	100µL-well	2 µL	0.005 mM
22DE	30µL-well	2 µL	0.005 mM
23ABC	30µL-well	2 µL	0.005 mM
23D	30µL-well	2 µL	0.01 mM
24	100µL-well	2 µL	0.01 mM
25	30µL-well	2 µL	0.01 mM
26	30µL-well	2 µL	0.01 mM
27	30µL-well	2 µL	0.01 mM
28	30µL-well	2 µL	0.01 mM
29	30µL-well	2 µL	0.01 mM
30	30µL-well	2 µL	0.01 mM
31	30µL-well	2 µL	0.01 mM

8.3 Uranyl acetate forms films over carbon holes

During this project, we used TEM microscopy to image filamentous proteins on TEM-grid-supported lipid monolayers. The formation of the TEM-grid supported lipid monolayers is described in section 3.4. To increase contrast, we transferred the lipid monolayer to a carbon grid with holes. The lipid monolayer is suspended over the carbon holes. The contrast was improved when imaging over carbon holes (figure 36 A). However, we observed covered holes in the control experiment without lipid (36 B). For this reason, we tested if covered holes can be found when fixating MilliQ water and F-buffer with uranyl acetate. We found no covered holes for MilliQ water (figure 36 D), however we did find in covered holes for F-buffer (figure 36 D). We conclude that uranyl acetate interacts with a component in the buffer that allows uranyl acetate to stabilise the suspended buffer.

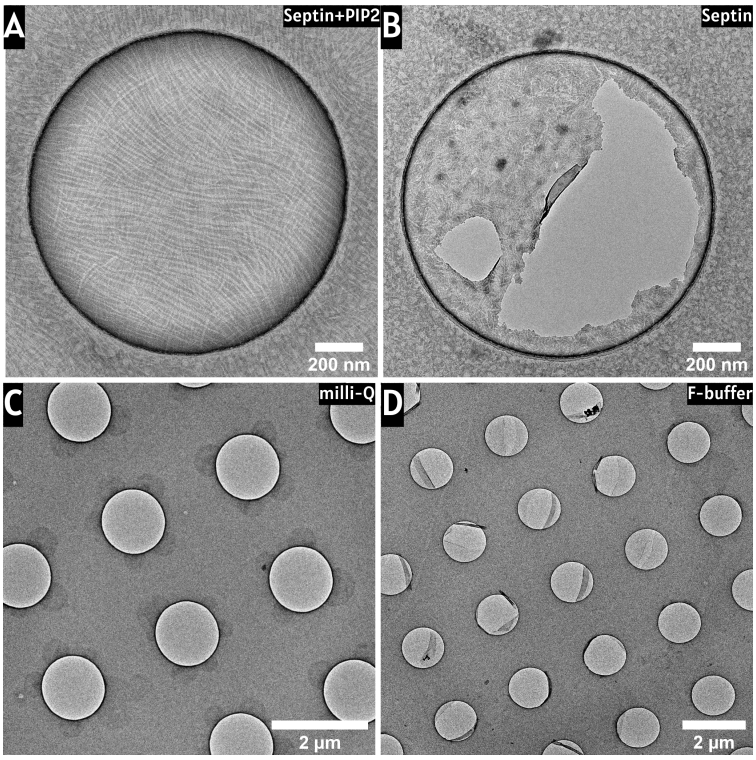

Figure 36: **Uranyl acetate can form covered holes.**(A) TEM image of 50 nM human septin hexamers on a 5% PIP_2 monolayer over carbon hole. (B) TEM image of 50 nM human septin hexamers over carbon hole. (C) TEM image of uranyl acetate stained MilliQ water. (D) TEM image of uranyl acetate stained F-buffer.